ATG9A and ATG2A form a heteromeric complex essential for autophagosome formation

Graphical abstract
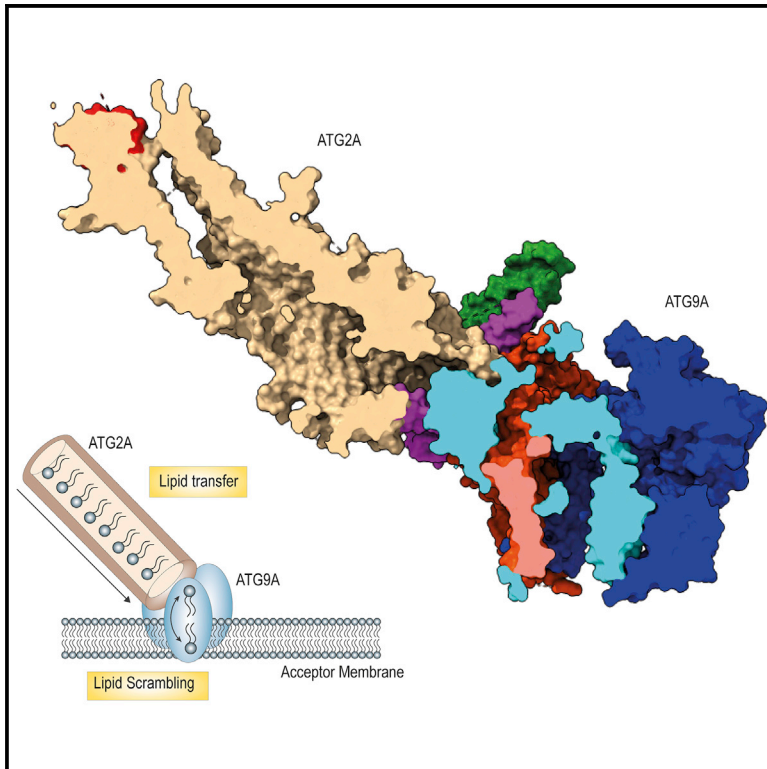
Authors

Alexander R. van Vliet,
George N. Chiduza, Sarah L. Maslen, ...,
J. Mark Skehel, Peter Cherepanov,
Sharon A. Tooze

Correspondence

sharon.tooze@crick.ac.uk

In brief

A critical aspect of autophagy is the membrane growth of the phagophore, a process that is still elusive. Here, we show that complex formation by the scramblase ATG9A and lipid transfer protein ATG2A is required for autophagy and characterize their interaction interface using structural mass spectrometry and EM techniques.

Highlights

- ATG9A and ATG2A form a heterotetrameric complex

- HDX and CXL-MS reveal intricate interaction interface between ATG9A and ATG2A

- Disrupting the ATG9A-ATG2A complex disrupts autophagic flux

- Lipid transfer tunnel of ATG2A binds proximal to the perpendicular branch of ATG9A

CellPress

Article

ATG9A and ATG2A form a heteromeric complex essential for autophagosome formation

Alexander R. van Vliet,[1,8] George N. Chiduza,[1,8] Sarah L. Maslen,[2] Valerie E. Pye,[3] Dhira Joshi,[4] Stefano De Tito,[1,5] Harold B.J. Jefferies,[1] Evangelos Christodoulou,[6] Chloë Roustan,[6] Emma Punch,[3] Javier H. Hervás,[1] Nicola O'Reilly,[4] J. Mark Skehel,[2] Peter Cherepanov,[3,7] and Sharon A. Tooze[1,9,*]

[1]Molecular Cell Biology of Autophagy, The Francis Crick Institute, London NW1 1AT, UK
[2]Proteomics Science Technology Platform, The Francis Crick Institute, London NW1 1AT, UK
[3]Chromatin Structure and Mobile DNA Laboratory, The Francis Crick Institute, London NW1 1AT, UK
[4]Peptide Chemistry Science Technology Platform, The Francis Crick Institute, London NW1 1AT, UK
[5]Institute of Experimental Endocrinology and Oncology (IEOS), National Research Council, Naples 80131, Italy
[6]Structural Biology Science Technology Platform, The Francis Crick Institute, London NW1 1AT, UK
[7]Department of Infectious Disease, Imperial College London, London W2 1NY, UK
[8]These authors contributed equally
[9]Lead contact
*Correspondence: sharon.tooze@crick.ac.uk
https://doi.org/10.1016/j.molcel.2022.10.017

SUMMARY

ATG9A and ATG2A are essential core members of the autophagy machinery. ATG9A is a lipid scramblase that allows equilibration of lipids across a membrane bilayer, whereas ATG2A facilitates lipid flow between tethered membranes. Although both have been functionally linked during the formation of autophagosomes, the molecular details and consequences of their interaction remain unclear. By combining data from peptide arrays, crosslinking, and hydrogen-deuterium exchange mass spectrometry together with cryoelectron microscopy, we propose a molecular model of the ATG9A-2A complex. Using this integrative structure modeling approach, we identify several interfaces mediating ATG9A-2A interaction that would allow a direct transfer of lipids from ATG2A into the lipid-binding perpendicular branch of ATG9A. Mutational analyses combined with functional activity assays demonstrate their importance for autophagy, thereby shedding light on this protein complex at the heart of autophagy.

INTRODUCTION

Macroautophagy, here referred to as autophagy, is a degradative pathway crucial for cell homeostasis and stress responses, whereby damaged organelles or protein aggregates are cleared or cellular material recycled. In conditions of nutrient starvation, mammalian target of rapamycin (mTOR) becomes inhibited leading to the subsequent activation of the ULK1/2 complex and the class III phosphatidyl inositol 3 kinase (PI3KC3) complex I, culminating in phagophore formation (Mercer et al., 2018; Morishita and Mizushima, 2019; Nishimura and Tooze, 2020).

One of the key events in autophagy is the nucleation and growth of the phagophore membrane, many aspects of which remain enigmatic (Melia et al., 2020). Autophagosome formation relies on a network of specific autophagy-related (ATG) proteins, of which ATG9A is the only transmembrane protein. ATG9A is synthesized in the ER before being transported to the Golgi complex (Young et al., 2006). Upon starvation, the bulk of ATG9A moves into vesicles that collectively form the ATG9A compartment and is not enriched in the nascent phagophore or autophagosome (Orsi et al., 2012). It is now debated whether these

ATG9A vesicles create the membrane seed of the nascent phagophore (Sawa-Makarska et al., 2020) or if ATG9A vesicles make transient contact, delivering components for recruitment of downstream autophagy machinery, and are then retrieved (Orsi et al., 2012; Judith et al., 2019; Karanasios et al., 2016). Recent data demonstrating lipid transport by ATG2A/B support the hypothesis that ATG9A and ATG2A facilitate expansion of the phagophore (Melia and Reinisch, 2022; Zhang et al., 2022). ATG9A, working as a lipid scramblase in the phagophore membrane, would assist in the equilibration of lipids delivered by ATG2A (Sawa-Makarska et al., 2020; Young et al., 2006; Orsi et al., 2012; Yamamoto et al., 2012).

Recently, cryoelectron microscopy (cryo-EM) studies of human ATG9A and its yeast ortholog revealed a novel trimeric lipid scramblase fold (Guardia et al., 2020; Maeda et al., 2020). The ATG9A trimer features a solvent accessible hydrophilic central pore, which spans the membrane bilayer and into which the lateral branch of each protomer opens. At each protomer interface, there are perpendicular branches, which are partly contiguous with the central pore, and connect the lateral branch to the cytosol (Maeda et al., 2020; Guardia et al., 2020). The structures
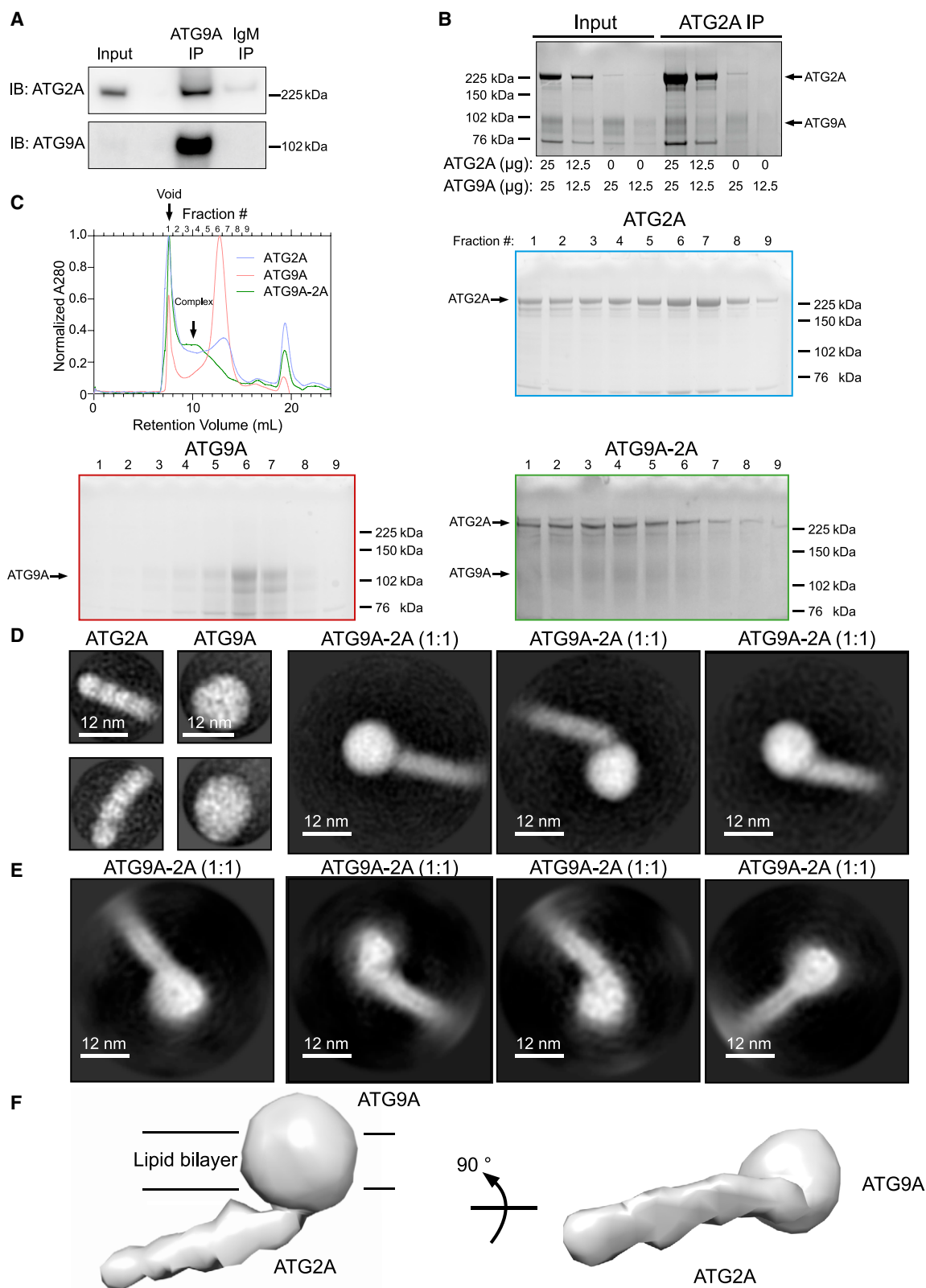
(legend on next page)

of two conformers (states A and B) and molecular dynamic (MD) simulations suggest that the central pore and lateral branches likely form a "funnel-like" solvent channel in the membrane (Maeda et al., 2020). Opening of the central pore into the membrane would allow lipid head groups to enter and flip-flop between the inner and outer leaflet of the bilayer (Maeda et al., 2020). Lipid binding to the lateral branch is thought to play a role in lipid scrambling; however, a detailed molecular mechanism is lacking (Matoba et al., 2020). The C terminus of the protein (residues 588–839) is mostly disordered and was not visualized in the cryo-EM structures (Guardia et al., 2020; Maeda et al., 2020).

ATG2A has been shown to mediate membrane tethering and lipid transfer (Chowdhury et al., 2018; Maeda et al., 2019; Valverde et al., 2019). The molecular mechanism of lipid transfer by ATG2A is currently based on low resolution structures and the crystal structure of a N-terminal fragment of the yeast Atg2 (Osawa et al., 2019). ATG2A was shown to form an elongated ~200 Å rod-like structure, with a hydrophobic cavity that spans the length of the structure, thought to be capable of accommodating the acyl chains of lipids. The C terminus of ATG2A contains two regions of relatively high conservation, the C-terminal localization region (CLR) and the ATG_C domain (Pfam:PF09333) (Chowdhury et al., 2018).

ATG2A-mediated lipid transfer between PI3P-containing membranes is stimulated by the Atg18/21 ortholog, WIPI4, which binds to ATG2A and PI3P in the phagophore membrane (Maeda et al., 2019; Chowdhury et al., 2018). The activity of ATG2A would generate asymmetry in the bilayer, necessitating ATG9A lipid scramblase activity to rectify the asymmetry (Valverde et al., 2019; Maeda et al., 2019; Chowdhury et al., 2018; Ghanbarpour et al., 2021). Although the direct interaction of ATG2A and ATG9A has been demonstrated (Ghanbarpour et al., 2021), the functional consequences for autophagy and their interaction interface remain to be determined. In yeast, putative Atg9 binding sites in Atg2 have been characterized and shown to be required for the localization and proper function of Atg2 at the tips of the phagophore. Based on sequence analysis, the homologous regions in ATG2A are speculated to play a similar role (Gomez-Sanchez et al., 2018). The aim of this work was to elucidate the molecular details and functional consequences of the ATG9A-2A complex.

RESULTS

In vitro reconstitution of the ATG9A-2A complex

To confirm previous results, we co-immunoprecipitated (coIP) endogenous ATG2A with endogenous ATG9A (Figure 1A) and used purified proteins to demonstrate direct ATG9A-2A interaction (Figure 1B). Size-exclusion chromatography (SEC) was used

to analyze the purified ATG9A trimer and ATG2A combined at a molar ratio of 1:3, respectively. Upon mixing, ATG9A and ATG2A co-eluted at a retention volume of ~10.4 mL, compared with the individual proteins, eluting at retention volumes of ~13.5 and 12.8 mL, respectively (Figure 1C), demonstrating that ATG9A and ATG2A can form a stable complex (Figure 1C). This was supported by the determination of a single melting temperature for the complex using nanoscale differential scanning fluorimetry (nanoDSF) which was consistent with two state unfolding (Figure S1A; Kopec and Schneider, 2011).

Negative stain transmission electron microscopy (NS-EM) was used to characterize the ATG9A-2A complex. Particles were picked from 1,847 micrographs and 2D classified, resulting in 5,870 (~26%) ATG2A rod-like particles, 4,327 (19%) globular ATG9A trimer particles, and 12,361 (~55%) crotchet shape (a musical note) particles composed of both a globular and rod-like part (Figures 1D and S1B). Similarly shaped particles were observed in the 2D class averages of vitrified samples, confirming the topology of the ATG9A-2A complex in solution (Figures 1E and S1C). 3D reconstruction could not be achieved reliably from the cryo-EM data due to conformational heterogeneity observed in particles of the complex (Figure S1D). However, a 3D reconstruction generated using images of negatively stained particles was consistent with the crotchet shaped particles in the cryo-EM classes (Figures 1E, 1F, and S1E). The rod-like part of the 3D reconstruction is ~240 Å in length and appeared bound to the globular structure (Figure 1F; EMD-B:EMD-15604).

Experimental validation of AlphaFold predictions of ATG2A and ATG9A

To interpret our NS-EM reconstruction of the ATG9A-2A complex, we validated AlphaFold (AF) models of ATG9A and ATG2A (Tunyasuvunakool et al., 2021). The most complete experimental ATG9A structure (PDB: 6WQZ) included amino acid residues (AA) 36–587 of the protein, spanning its highly conserved region (ATG9 core domain, Pfam:PF04109). Some features of the cryo-EM map, corresponding to the C-terminal region of ATG9A (from AA 587), were not modeled due to lower local resolution (Guardia et al., 2020). The AF prediction (AF-Q7Z3C6-F1-model_v1), which had good agreement with the experimental structure (Cα RMSD = 0.57 Å over 552 AA), predicted that the C-terminal residues 636–656 and 695–723 could adopt an α-helical conformation and interact with the folded N-terminal core (Figure S2A).

We performed chemical crosslinking coupled with mass spectrometry (CXL-MS) of ATG9A to further validate the AF model. We used disuccinimidyl dibutyric urea (DSBU) that crosslinks lysine and less frequently serine, threonine, and tyrosine residues (Table S1). The Euclidean distance cutoff used, 36.5 Å,

---

Figure 1. ATG9A-ATG2A form a heterotetrameric complex

(A) Endogenous ATG2A co-immunoprecipitated (coIP) from cells with endogenous ATG9A.

(B) *In vitro* purified ATG9A coIP with purified ATG2A (Coomassie blue stain [CB]).

(C) Size-exclusion chromatograms (SECs) of ATG9A (red), 2A (blue) and the complex (green). Indicated fractions were analyzed by CB.

(D) 2D class averages of ATG9A, 2A and their complex from negative stain EM micrographs.

(E) 2D class averages of ATG9A-2A complex from cryo-EM.

(F) 3D reconstruction of ATG9A-2A complex from NS-EM of the ATG9A-2A complex.
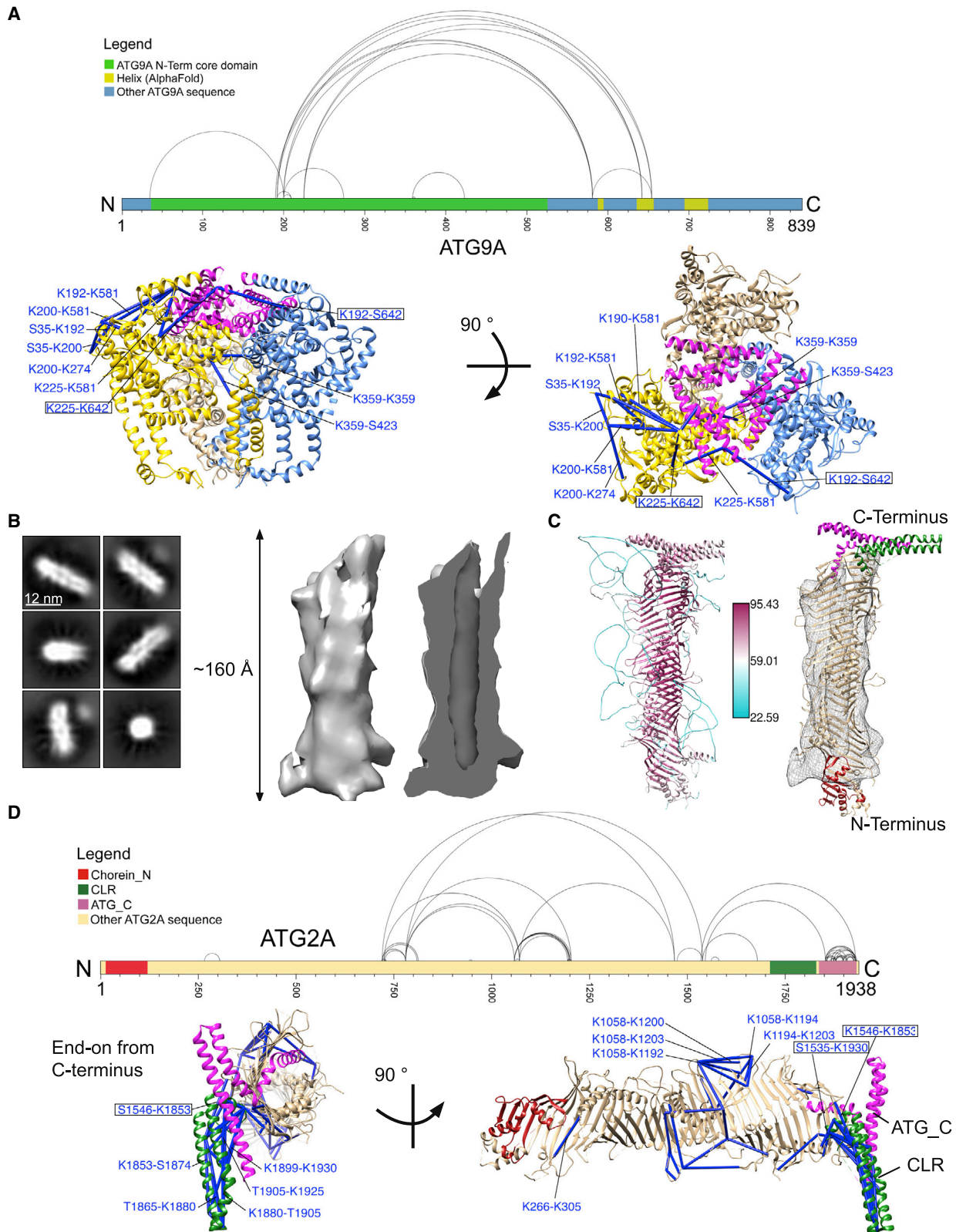
was calculated as recommended (Orbán-Németh et al., 2018; Pan et al., 2018), by summing the extended length of the cross-linker reactive residues, the crosslinker and 13 Å to allow for conformational dynamics. Crosslinks longer than 36.5 Å but less than 50 Å that are not satisfied in the AF conformation may be satisfied in alternative conformations in solution (Orbán-Németh et al., 2018; Pan et al., 2018), whereas crosslinks longer than 50 Å were not taken forward. Crosslinks were detected between the AF predicted ATG9A C-terminal helices and ATG9 core domain, specifically K192-S642 (35.0 Å), K225-S642 (31.5 Å), and K225-S654 (36.5 Å) which when mapped onto the AF model are within 36.5 Å (Figure 2A; Table S2), and a crosslink between K200-S642 (40.3 Å) which is within 50 Å and is potentially satisfied in an alternate conformation of this dynamic region of ATG9A (Figure S2B; Table S2).

Cryo-EM was used to image vitrified samples of recombinant ATG2A, and the resulting 3D reconstruction, refined to ~15 Å resolution, revealed a ~160 Å rod-like structure, with a cavity running along its entire length (Figures 2B and S2C–S2E; EMD-B:EMD-15605). Docking of the AF model of ATG2A (AF-Q2TAZ0-F1-model_v1) into the cryo-EM map supported the overall topology of the protein including the proposed lipid transfer cavity (Figure 2C). Our cryo-EM data and the predicted atomic model were consistent with the published NS-EM 3D reconstruction of ATG2A; however, the NS map accounts for more of the protein than our cryo-EM map, specifically parts of the Chorein_N (Pfam:PF12624) and CLR domain (Figure S2F; Chowdhury et al., 2018). The predicted ATG2A model is comprised almost entirely of β strands folded into a β helix with a right-handed helical pitch, open along its length with the β sheets lining the walls of the putative lipid transfer cavity. Most of the predicted α helices are found in loops with low confidence scores (predicted Local Distance Difference Test [pLDDT] < 50), except for the α helices comprising the C-terminal CLR and ATG_C domains (pLDDT > 50) (Figure 2C). Despite the intermediate confidence of the prediction in the CLR and ATG_C domains, they were not accounted for in our single particle analysis, suggesting flexibility in the region and potential folding on interaction (Figure 2C). However, CXL-MS of ATG2A using DSBU revealed several satisfied crosslinks (≤36.5 Å) (Figure 2D; Table S2) as well as potential crosslinks in alternate conformations (>36.5 Å and <50 Å) (Figure S2G; Table S2), within the ATG_C domain suggesting a compact and dynamic fold rather than an extended random coil. Together with crosslinks between S1535-K1930 (11.1 Å) and K1546-S1853 (26.9 Å) connecting the ATG_C and the rod-like domain, the CXL-MS data support the predicted folding of this region in ATG2A, consistent with the AF model (Figures 2D and S2G).

Based on the docking of these AF models, we propose that a single ATG2A subunit binds one ATG9A trimer (Figure S2H). This conclusion is consistent with a molecular weight estimation of ~496 kDa based on the migration of the crosslinked complex on SDS-PAGE (Figure S2I). The docked AF models do not contact each other suggesting the conformation of the proteins predicted by the AF models may differ to that determined by NS-EM.

Identification of ATG9A binding sites on ATG2A

Given the low resolution of our 3D reconstruction, we used mutagenesis coupled with peptide arrays to map the ATG9A-2A interface. We generated four roughly equal fragments of ATG2A spanning residues 1–482, 483–973, 974–1,453, and 1,454–1,938 (designated as fragments 1–4) and tested each for ATG9A binding using coIP (Figure 3A). ATG9A primarily bound to fragment 4 of ATG2A, which includes the CLR and ATG_C domains (Figure 3B). A peptide array of fragment 4 was generated and probed with purified 3xFlag-ATG9A (Figure 3C), which identified two putative ATG9A binding sites that have a Gaussian-like distribution (schematically illustrated in Figure S3A). Binding site 1 (ATG2A S1) spanned residues 1,585–1,604, and site 2 (ATG2A S2) residues 1,760–1,779 (Figures 3C, S3A, and S3B). ATG2A S1 shares homology with the Atg9 binding site in yeast (Figure S3C; Gomez-Sanchez et al., 2018). S2 is localized in the C-terminal CLR domain (residues 1,723–1,829), shown to be critical for autophagy (Velikkakath et al., 2012). Interestingly, both sites are located close to the C-terminal opening of the lipid transfer cavity (Figure S3B). To validate these sites, we deleted them in fragment 4 of ATG2A and used these mutants to coIP ATG9A (Figure S3D). ATG9A binding was not reduced by deleting ATG2A S1 but decreased ~70% by deleting ATG2A S2 (Figure S3D). Based on this, we focused on S2 as a potential ATG9A binding site. Subsequent deletion of S2 in full-length ATG2A (ATG2A ΔS2) caused a similar reduction of approximately 70% in ATG9A binding (Figure 3D). These data indicate that ATG2A can bind ATG9A through its C terminus via residues in the CLR domain. Previous work showed ATG2A binds membranes through an amphipathic helix (AH) region in the CLR, and mutation of key residues in this AH that abolished membrane binding also abolished autophagy (Tamura et al., 2017). Note, these mutations were between AA 1,732–1,767 and partially overlap with ATG2A S2. To disentangle membrane binding from ATG9A binding, we tested ATG9A binding to the ATG2A CLR mutant (AH-E) with impaired membrane association (Tamura et al., 2017). ATG2A AH-E interacted with ATG9A to the same extent as WT ATG9A suggesting that residues in the CLR required for membrane binding are different to those

---

Figure 2. Validation of AF models of ATG9A and ATG2A

(A) Top, intraprotein crosslinks (gray lines) of ATG9A mapped onto the primary structure. Green: the sequence covered by the experimentally solved structure (state A; PDB: 6WQZ), Gold: regions structured only in the AF model, Blue: uncharacterized. Bottom, intraprotein crosslinks (blue < 36.5 Å) mapped on to the AF model of ATG9A. Regions in state A are shown in tan, gold, and blue, whereas regions structured only in AF model are in magenta.

(B) 2D class averages, 3D reconstruction, and a cross-section of this reconstruction from cryo-EM micrographs of ATG2A.

(C) Left, full-length AF model of ATG2A shown as a ribbon colored by per residue pLDDT score. Right, AF model of ATG2A with low pLDDT (<50) regions removed, docked into the experimental 3D reconstruction (mesh) from cryo-EM.

(D) Top, intraprotein crosslinks (gray lines) of ATG2A mapped onto its primary structure scheme. Bottom, intraprotein crosslinks (blue < 36.5 Å) mapped on to the AF model of ATG2A. ATG2A AF colored by domain; Chorein_N: red, CLR: magenta, and ATG_C: green.
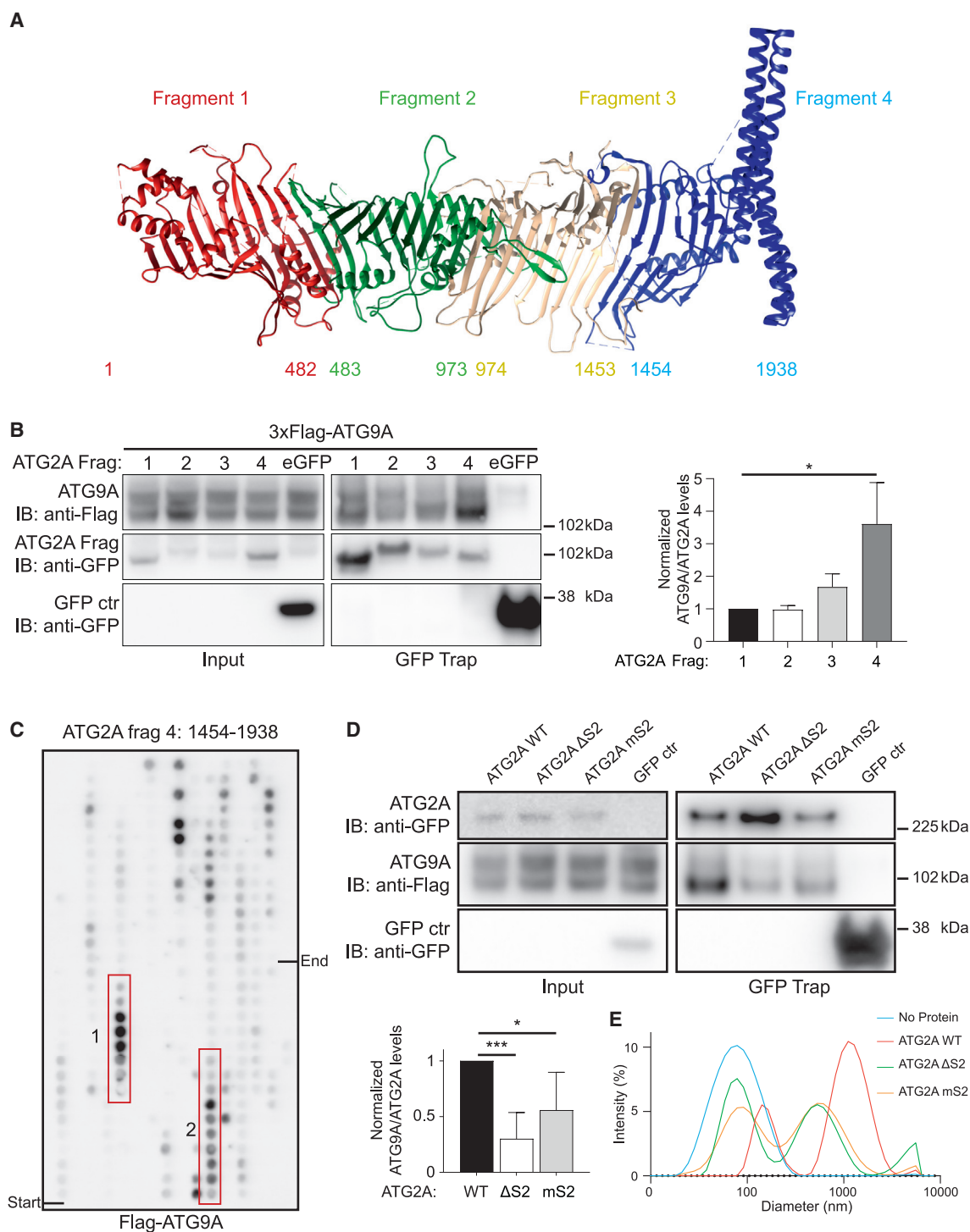
Figure 3. Mapping the binding sites of ATG9A in ATG2A

(A) AF model of ATG2A with low pLDDT (<50) regions removed, colored by fragments used in (B). (B) Immunoblot showing coIP from cells of 3xFlag-ATG9A using GFP-ATG2A fragments. Quantification of the relative ATG9A levels (mean ± SD; n = 3, *p < 0.05; one-way ANOVA with Dunnett's multiple comparison). The contrast for the immunoblot for GFP control (ctr) has been adjusted for clarity.

(C) Peptide array of fragment 4 of ATG2A incubated with ATG9A.

(D) Immunoblot of coIP performed from cell extracts of 3xFlag-ATG9A using GFP-ATG2A WT, ΔS2 or mS2 and the quantification of relative ATG9A levels (mean ± SD, n = 6, *p < 0.05 ***p < 0.001; Student's t test).

(E) Liposome tethering assay with 3xFlag-tagged proteins as indicated added to small unilamellar vesicles and the size measured using dynamic light scattering (DLS) (n = 3).
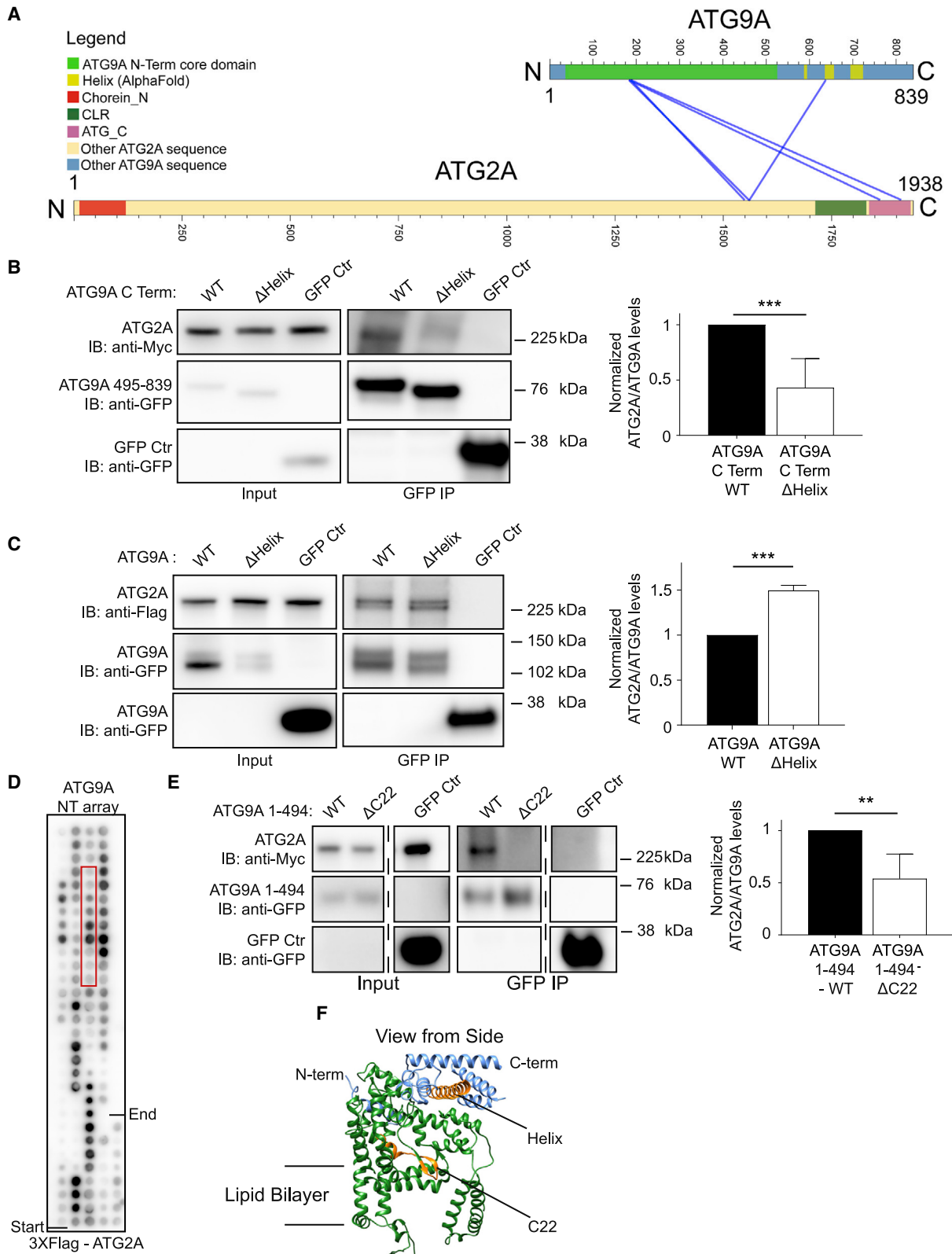
(legend on next page)

required for ATG9A binding (Figure S3E). Next, we explored what residues within ATG2A S2 could be important for ATG9A binding. A mutational array of the S2 sequence showed reduced ATG9A binding when charged residues D1763, E1770, R1773, K1774, D1775, and R1777 were mutated to other residues except ones that conserved the charge (Figure S3F). The role of these ATG2A residues for ATG9A binding was confirmed by reduced coIP when E1770, R1773, K1774, D1775, and R1777 were all mutated to alanine (ATG2A mS2) (Figure 3D). Note, both ATG2A ΔS2 and ATG2A mS2 had a reduced capacity to tether liposomes *in vitro* compared with ATG2A WT (Figure 3E). Combined with the results of the ATG2A AH-E experiments, this suggests that ATG2A does not require membrane binding to bind ATG9A, but the interface in ATG2A which binds ATG9A is important for its membrane binding. This result also indicates that both membrane binding and ATG9A binding may be fundamental for the functioning of this complex and should be further investigated in future work.

Identification of ATG2A binding sites on ATG9A

As a multi-spanning transmembrane protein, ATG9A is challenging to subdivide; hence, we used CXL-MS with DSBU to map its interface with ATG2A. CXL-MS of the complex identified 177 unique crosslinks, with 22 being ATG9A and ATG2A interprotein crosslinks (Table S1). These crosslinks indicated that the interaction between the two proteins is mediated by the N and C termini of ATG9A: crosslinks from residues 192, 200, 581, and 642 in ATG9A to residues 1,539, 1,546, 1,880, and 1,930 in the C terminus of ATG2A (Figure 4A; Table S2). These results validate our analysis of ATG9A binding sites in the C terminus of ATG2A (Figure 3). CXL-MS results for ATG9A suggested putative binding sites for ATG2A on ATG9A were in the ATG9 core domain and C terminus (Figure 4A). To investigate this further, we made deletion constructs of ATG9A, removing the C terminus of the protein (constructs spanning AA 1–494 and 1–522) to test if this abolished ATG2A binding. Both constructs retained ATG2A binding (Figure S4A), consistent with the CXL-MS (Figure 4A), suggesting additional ATG2A binding sites in the ATG9 core domain.

We mapped the ATG2A binding interface by first addressing the C-terminal binding site(s) with peptide arrays spanning the C terminus (AA 495–839) of ATG9A. Binding of recombinant 3xFlag-ATG2A yielded several potential interaction sites on ATG9A (Figure S4B), but mutagenesis of these ATG9A sites had no effect on ATG2A binding (data not shown). We then compared the peptide array hits with our CXL-MS and AF predictions of ATG9A's C terminus. Based on this, we identified a

putative α helix (AA 695–723) in the C terminus of ATG9A. Deletion of this helix in the ATG9A C-terminal domain (AA 495–839) resulted in reduced ATG2A binding (Figure 4B). However, deletion of this helix in the context of full-length ATG9A protein increased ATG2A binding (Figure 4C). All together, we conclude that the C terminus of ATG9A could modulate ATG2A binding and plays only a minor role in the putative interaction interface.

Next, we focused on the ATG9 core domain of ATG9A. In the CXL-MS, the crosslinks involving residues 192 and 200 in ATG9A mapped to residues 1,546, 1,880, and 1,930 in ATG2A (Figure 4A; Tables S1 and S2). We used peptide arrays spanning part of the cytosolic N-terminal core (ATG9A 152–298, ATG9A NT array) and probed it with purified 3xFlag-ATG2A (Figures 4D and S4C). Like the C-terminal peptide array, the N-terminal peptide array did not yield a single strong candidate for the ATG9A interaction site (Figure 4D). Nonetheless, deletion of all plausible hits from the peptide array (data not shown), yielded one site which reduced ATG2A binding (Figure 4E). Deletion of this site (termed C22), spanning ATG9A residues 233–252, caused an approximate 50% reduction in ATG2A binding (ATG9A ΔC22, Figure 4E). The location of both the C-terminal α helix (AA 695–723) and the N-terminal residues spanning residues 233–252 are shown on the AF model of the ATG9A protomer (Figure 4F). These data support the identification of one major binding site in the N-terminal core of ATG9A, and a secondary site influencing binding in the C terminus of ATG9A.

Functional importance of ATG9A-2A binding

To test the effect of abolishing ATG9A-2A binding on autophagy, we used ATG2A/B CRISPR-Cas9 double knockout (DKO) cell lines (Valverde et al., 2019) and stably expressed either ATG2A WT or ATG2A ΔS2 and compared these with empty vector (EV) transfected ATG2A/B DKO cells (Figures 5A and S5G). In ATG2A/B DKO cells, as previously reported (Valverde et al., 2019), lipidated LC3B (LC3B-II) accumulated in fed conditions (Figure 5A); neither starvation nor starvation with Bafilomycin A1 (Baf A1), which inhibits lysosomal degradation, increased LC3B levels, indicating a failure to undergo autophagic flux. Autophagy flux was rescued with ATG2A WT but not ATG2A ΔS2 (Figure 5A). To investigate whether this was solely due to reduced ATG9A binding, we purified ATG2A ΔS2 and confirmed it retained lipid transfer activity, albeit ~2.5-fold slower than WT, an effect which was compensated by increasing amounts of protein (Figures S5A–S5F). As shown above, ATG2A ΔS2 also had reduced liposome tethering compared with ATG2A WT, consistent with the slower transfer rate (Figure 3E). Membrane binding

---

Figure 4. Mapping binding sites of ATG2A in ATG9A

(A) Interprotein crosslinks between ATG9A and 2A in complex.

(B) Immunoblot of coIP performed from cell extracts of myc-ATG2A with WT or ΔHelix GFP-ATG9A C-terminal fragment (AA 495–839), quantification, right (mean ± SD; n = 4, ***p < 0.001; Student's t test).

(C) Immunoblot of coIP performed from cell extracts of 3xFlag-ATG2A with WT or ΔHelix GFP-ATG9A, quantification, right (mean ± SD; n = 3, ***p < 0.001; Student's t test).

(D) Peptide array spanning N-terminal sequence of ATG9A (AA 152–298) incubated with ATG2A.

(E) Immunoblot of coIP performed from cell extracts of 3xFlag-ATG2A using loop mutants (C22, AA 233–252) in GFP-ATG9A N terminus (AA 1–494). Blot shows monomer of each construct. Dashed lines indicate cropped blot. Quantification, right (mean ± SD; n = 4, **p < 0.01; Student's t test).

(F) Schematic overview of helix and C22 residues mapped on the AF model of ATG9A.

A

B

C

D

E
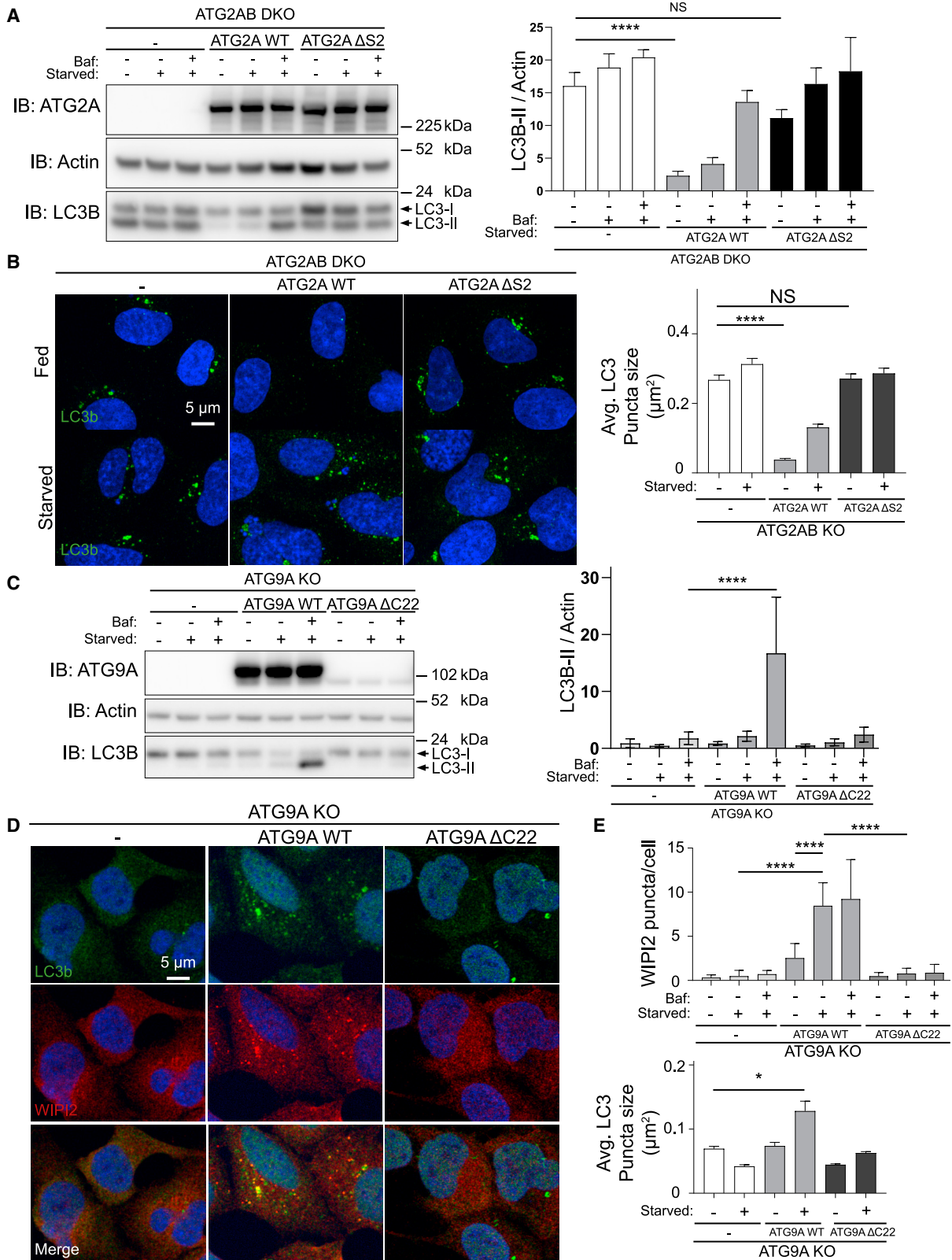
(legend on next page)

by the CLR is required for autophagy; hence, we could not fully conclude that the failure of ATG2A ΔS2 to rescue is only due to reduced ATG9A binding.

EV transfected ATG2A/B DKO cells, as previously shown (Valverde et al., 2019; Velikkakath et al., 2012), displayed an accumulation of abnormally large LC3B-positive structures, which were resolved upon stable expression of ATG2A WT but not when expressing ATG2A ΔS2 (Figure 5B). Starvation did not increase LC3B puncta in EV control and mutant expressing cells compared with ATG2A WT. These results agree with previous reports showing that ATG2A's CLR domain is required to rescue autophagy in cells lacking ATG2A/B (Velikkakath et al., 2012).

We used CRISPR-Cas9 KO cells for ATG9A (ATG9A KO) to generate stable cell lines expressing either EV, ATG9A WT or ATG9A ΔC22 (Figure 5C). ATG9A KO cells did not have large LC3B positive structures in fed conditions (Figure S5H) and had no increase in LC3B-II levels after starvation with or without Baf A1 indicating a failure to induce autophagy (Figure 5C). In starved cells, ATG9A WT, but not ATG9A ΔC22, rescued autophagic flux (Figures 5C and 5D). Likewise, LC3B and WIPI2 puncta were rescued in ATG9A WT cells but not with ATG9A ΔC22 expressing cells (Figures 5D and 5E). ATG9A ΔC22 lacked the typical Golgi glycosylated form of ATG9A (Figure S6C) but still displayed Golgi localization in stable expressing cells (Figure S5I). ATG9A ΔC22 levels were higher than endogenous ATG9A, but significantly lower than ATG9A WT (Figure S6A). To confirm that the reduced autophagic flux was due to the mutation of ATG9A ΔC22 and not expression level we repeated the starvation time course using transiently transfected cells with roughly equal expression and confirmed that autophagy was blocked in ATG9A ΔC22 expressing cells (Figure S6B). Additionally, to confirm the effect on autophagic flux was due to the abolishing of ATG2A binding, we purified ATG9A ΔC22 and confirmed that it was folded and retained scramblase activity (Figures S6C–S6H).

Combined, these results indicate that interaction between ATG9A and ATG2A is required for autophagic flux and mutating residues required for binding blocks autophagic flux.

Integrative modeling of the ATG9A-2A complex

To elucidate the full ATG9A-2A interaction interface, we utilized hydrogen-deuterium exchange MS (HDX-MS). The mass difference (Dmass) between the peptic peptides from ATG9A and ATG2A were compared with the equivalent peptides derived from the complex. Analysis of the results was done by applying a solvent accessibility model, in which regions at the interaction interface should have reduced solvent accessibility compared with peptides from ATG9A or 2A alone (see Figure S7A and Table S3; de Vries et al., 2010). In total, 185 ATG9A peptides were recovered, a sequence coverage of 81.2% (Figure S7A; Table S3). Three ATG9A regions showed protection from deuterium exchange in the complex with ATG2A at or above the 95% confidence intervals: 220–240 (9A HDX S1), 363–373 (9A HDX S2), and 437–454 (9A HDX S3), with protection peaking at 3,000 s. 578–602 (9A HDX S4) showed significant protection only at 30 s suggesting a more dynamic ATG2A interaction (Figures 6A and 6B). 9A HDX S1 overlapped with the ATG9A C22 site and mutating residues in S1 (AA 220–240, mHDX S1) to alanine reduced ATG2A binding, supporting our data that this region forms part of the interface with ATG2A (Figures 4D, 4E, and S7C). 9A HDX S2 is close to the membrane and could be solvent accessible through the perpendicular branch at the trimer interface and therefore unlikely to be part of the interaction interface. Protection of 9A HDX S2 suggests that ATG2A binding reduces the solvent accessibility of the perpendicular branch (Figures 6B, 7B, and 7C). In the AF model, 9A HDX S3 is partially covered by the predicted C-terminal α helix (AA 695–723), and the deletion of this helix increased ATG2A binding to ATG9A (Figure 4C). Mutation of residues in 9A HDX S3 (AA 437–454, mHDX S3) to alanine lead to reduced interaction with ATG2A (Figure S7C). The potential rearrangement of structural elements such as this α helix in the C terminus of ATG9A upon ATG2A binding is consistent with the apparent increased solvent accessibility of part of this region (AA 764–784) (Figure 6A).

291 peptides were recovered for ATG2A, spanning 89.4% of its amino acid sequence (Figure S7B; Table S4). Many regions displayed reduced hydrogen-deuterium exchange in the presence of ATG9A, with 1,736–1,757 (2A HDX S1) showing the greatest extent of protection in the presence of ATG9A (Figure 6C). This region is 3 amino acid residues away from ATG2A S2 (AA 1,760–1,779), suggesting that this region is protected due to interaction with ATG9A. The remaining protected peptides are in the loop regions lining the opening of the putative lipid transfer cavity, suggesting that binding of ATG2A to ATG9A induces conformational changes along the length of the lipid transfer cavity (Figure 6D).

Finally, using ATG9A HDX S1, S2, and S4 together with ATG2A HDX S1 as "active residues" and residues 192, 200, and 642 in ATG9A, 1,539, 1,546, 1,880, and 1,930 in ATG2A as "passive

Figure 5. Impairing ATG9A-2A interaction impairs autophagy
(A) Immunoblot of ATG2AB DKO cells stably expressing either empty vector (-), ATG2A WT, or ATG2A ΔS2. Cells were in full medium (fed), starvation medium (Starved), or starvation medium with Bafilomycin A1 (Baf A1). Right, quantification of LC3B-II levels/actin. Mean ± SD; n = 3, ****p < 0.0001; one-way ANOVA with Dunnett's multiple comparison).
(B) ATG2AB DKO cells stably expressing either empty vector (-), ATG2A WT, or ATG2A ΔS2. Cells were in full medium (fed) or starvation medium (Starved) and fixed and labeled for LC3B. Quantification was of LC3B-II puncta average size. Mean ± SEM; n = 3, ****p < 0.0001; one-way ANOVA with Dunnett's multiple comparison.
(C) Immunoblot of ATG9A KO cells stably expressing either empty vector (-), ATG9A WT, or ATG9A ΔC22. Cells were in full medium, starvation medium (Starved), or starvation medium with Bafilomycin A1 (Baf A1). Right, quantification of LC3B-II levels/actin. Mean ± SD; n = 3, ****p < 0.0001; one-way ANOVA with Dunnett's multiple comparison.
(D) ATG9A KO cells stably expressing empty vector (-), ATG9A WT, or ATG9A ΔC22. Cells were starved (Starved), fixed, and labeled for LC3B and WIPI2.
(E) Quantification of WIPI2 puncta and average LC3B-II puncta size (D; Figure S5H) (mean ± SD for WIPI2 analysis and mean ± SEM for LC3B; n = 3, *p < 0.05, ***p < 0.001, ****p < 0.0001; one-way ANOVA with Dunnett's multiple comparison).

A Exposure with ATG2A

Orange: 30 seconds
Blue: 300 seconds
Black: 3000 seconds

Protection with ATG2A

220-240
9A HDX S1

9A HDX S2

9A HDX S3

9A HDX S4

B

9A HDX S4
9A HDX S3
9A HDX S1
9A HDX S2

Exposed
Protected

Lipid Bilayer

90°

ATG9A view from top

C Exposure with ATG9A

Orange: 30 seconds
Blue: 300 seconds
Black: 3000 seconds

Protection with ATG9A

2A HDX S1

D

ATG2A view from side

Exposed
Protected

ATG2A view from back

90°

2A HDX S1

(legend on next page)

residues,'' the AF models of both ATG9A and ATG2A were docked using HADDOCK (Figures 7A and S8; de Vries et al., 2010). To validate the top scoring model, the presence of ATG9A HDX S3 and ATG2A S2 at the predicted interface as well the distance constraints from the CXL-MS were measured (Figures S8A and S8B; Table S2; Video S1). However, HDX-MS and mutagenesis provided a more robust validation for the model since in both proteins some crosslinked residues are in potentially dynamic loop regions.

In our model of ATG9A-2A, ATG2A makes extensive contact with one protomer of ATG9A (orange in Figure 7B) through its CLR domain creating an interface with a buried surface area of ~1,700 Å^2 including residues in 9A HDX S1 and S3. ATG2A also contacted the adjacent protomer creating an interface of ~600 Å^2 (cyan in Figure 7B). This second predicted interface in ATG2A was mediated by a structured but potentially flexible loop region (AA 1,681–1,700, 50 > pLDDT < 70) flanked by regions 1,665–1,677 and 1,707–1,726 which may be dynamic (Figure 6C, ATG9A-2A_AF.pdb). The AF predicted C-terminal helices of ATG9A (residues 636–638 and 720–723) play a limited role in the interaction with ATG2A's CLR domain with most of the predicted contacts located in ATG9A where 9A HDX S1 and S3 are (Figure 7; ATG9A-2A_AF.pdb). In our final model of ATG9A-2A, the opening of the putative lipid transfer cavity in the N-terminal chorein_N domain of ATG2A is facing away from the membrane where ATG9A is embedded (Figures 7A and 7B). The C-terminal opening of the putative lipid transfer cavity, continuous with the CLR domain, is proximal to the membrane and the perpendicular branch of ATG9A thought to be involved in lipid binding (Figure 7C).

DISCUSSION

Our study characterizes the molecular details of the ATG9A-2A protein complex that plays a central role in phagophore expansion. Direct interaction between ATG9A and ATG2A was shown in yeast and mammalian proteins (Ghanbarpour et al., 2021; Gomez-Sanchez et al., 2018). The N-terminal domain of ATG2A (AA 237–431) was shown to be required for interaction with ATG9A (Tang et al., 2019), whereas more recent studies show interaction with the C terminus of Atg2/ATG2A (Gomez-Sanchez et al., 2018; Ghanbarpour et al., 2021; Kotani et al., 2018; Guardia et al., 2020). Here, we identify a region of ATG2A (S1: AA 1,585–1,604) homologous to the Atg9 binding region in yeast Atg2 and proximal to ATG9A-2A interprotein crosslinks in our CXL-MS data. However, mutagenesis of ATG2A S1 did not significantly affect the binding to ATG9A, suggesting that the ATG9A-2A interfaces in yeast and mammals may not be identical (Gomez-Sanchez et al., 2018). Our HDX-MS data showed increased exposure of ATG2A AA 1,665–1,677 suggesting that this region undergoes a conformational change upon ATG9A binding. This region is homologous to a putative yeast binding region (see Figure S3C), which has been speculated to play an allosteric and modulatory role in ATG9A-2A interactions (Gomez-Sanchez et al., 2018). The novel ATG9A interacting regions we identify, ATG2A S2 and ATG2A HDX S1, are in the CLR. Our data identify a function for this previously described autophagy essential region of the protein (Velikkakath et al., 2012). Deletions of regions in yeast CLR (AA 1,321–1,427) reduce interaction with Atg9 suggesting that this interaction may be conserved (Kotani et al., 2018).

Stable rescue of ATG2A WT in ATG2 DKO cells restored autophagy flux, whereas ATG2A ΔS2 expression failed to do so. ATG2A ΔS2 was folded and could transfer lipids in vitro at a rate approximately 2.5 times less than the wild type, which can be explained by a reduction in membrane tethering. Both impaired ATG9A binding, and the reduction in membrane tethering may explain the lack of rescue with ATG2A ΔS2 (Figure 5A). Previous data have shown that reduced lipid transfer of an ATG2A mutant in vitro can be compensated by higher expression in cells (Valverde et al., 2019). We note expression of the ATG2A ΔS2 mutant in stable cell lines was higher than endogenous ATG2A (Figure S5G), which could have compensated for the slower lipid transfer rate; however, there was still no rescue of flux (Figure 5A). Similarly, an ATG9A mutant with impaired ATG2A binding (ATG9A ΔC22) could not rescue autophagy flux in ATG9A KO cells (Figure S6B). We conclude that the failure of ATG9A ΔC22 to rescue autophagic flux is likely due to the impaired interaction with ATG2A. In both mammals and yeast, impairing ATG9A-2A interaction impairs autophagy, supporting our conclusion that the interaction with ATG9A is responsible for the proper function of ATG2A at phagophore membranes and is essential for autophagy (Velikkakath et al., 2012; Kotani et al., 2018; Gomez-Sanchez et al., 2018).

Our HDX-MS data suggest the conformational changes induced in ATG2A by ATG9A binding are transmitted throughout the length of the protein. Such conformational changes have been speculated to explain the observation in yeast that binding of Atg2 to Atg9 increased Atg18 (WIPI ortholog) binding to Atg2. There is significant protection to deuterium exchange in the AF predicted loop region of ATG2A (1,344–1,357) adjacent to the WIPI4 interacting region (1,358–1,404); however, there is no evidence for ATG9A facilitating WIPI4 binding to ATG2A (Gomez-Sanchez et al., 2018; Kotani et al., 2018).

Mapping the ATG2A interacting regions in ATG9A provided evidence of ATG2A binding mainly through the highly conserved ATG9 core domain rather than the less conserved and mostly disordered C-terminal region (AA 522–839) (Guardia et al., 2020). Using CXL-MS, we validated the AF prediction of ATG9A which suggests that short, interspersed regions of the C terminus fold and interact with the ATG9 core domain, supporting previous data (EMDB:EMD-21874) (Guardia et al., 2020). By experimentally validating the AF model of ATG9A, we provide a more complete atomic model of ATG9A. In our

---

Figure 6. HDX-MS of the ATG9A-2A complex
(A and C) Mass difference (Dmass) plots of ATG9A (A) and ATG2A (C) compared with ATG9A-2A sample at different time points (30, 300, and 3,000 s). Blue (protected in complex) and red (exposed in complex) dashed lines are 95% confidence thresholds.
(B and D) Dmass for the 300 s time point mapped onto the AF models of ATG9A (B) and ATG2A (D). Regions for which no peptides were detected in the experiments are shown in gray. HDX sites identified as significant are indicated.
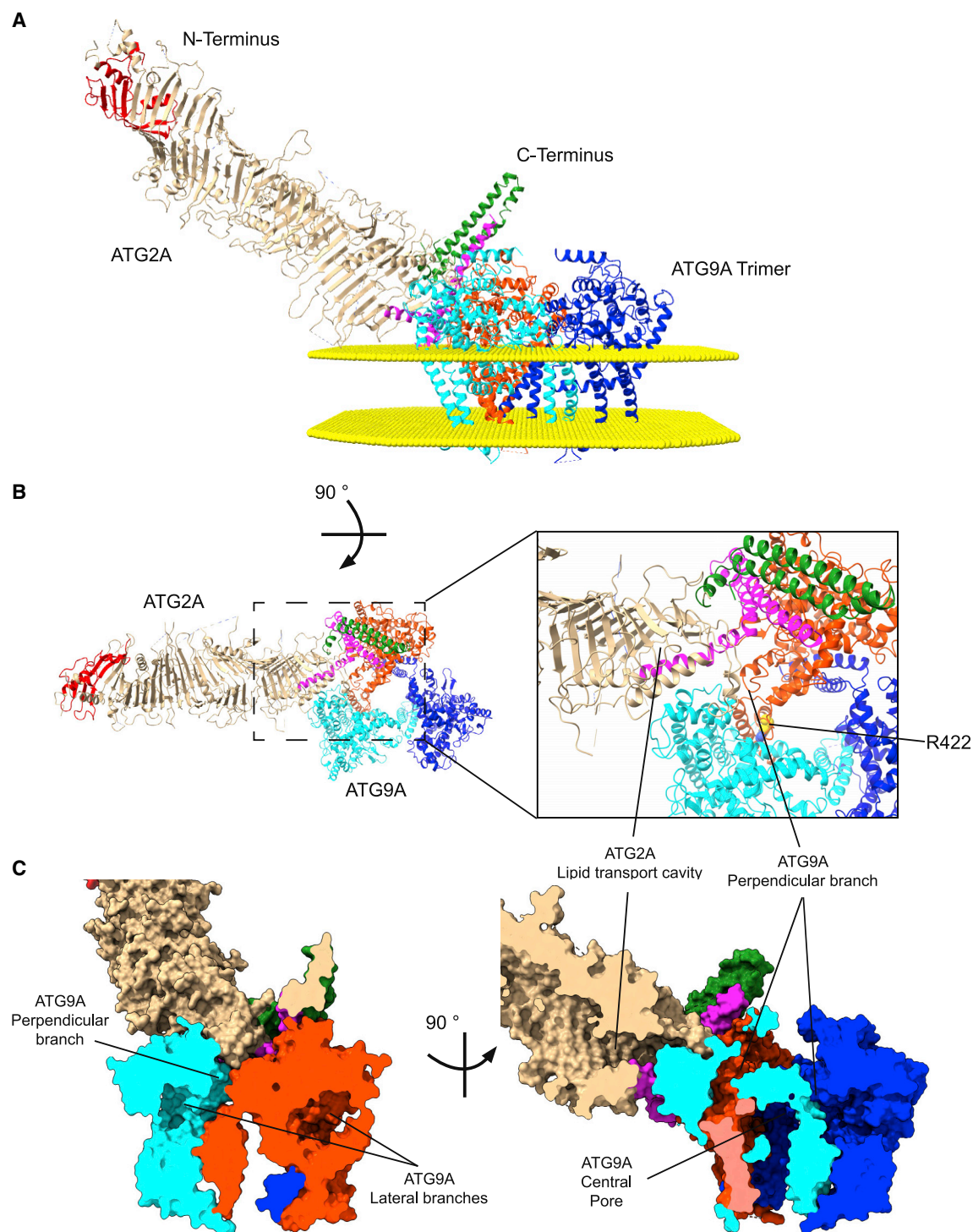
Figure 7. Model of the ATG9A-2A complex

(A) ATG2A shown in tan with Chorein_N, CLR, and ATG_C domains shown in red, magenta, and green, respectively. ATG9A protomers are shown in orange, cyan, and blue and the membrane as gold spheres.

(B) Close up of putative ATG9A-2A interface. R422, identified previously (Guardia et al., 2020), in the perpendicular branch of ATG9A shown as spheres colored by heteroatom.

(C) Slice through of ATG9A-2A isosurface representation of the HADDOCK model showing the putative lipid transfer cavity of ATG2A, and the perpendicular branch adjacent to the interaction interface.

predictive atomic model of the complex, ATG2A binds at the protomer interface, placing the opening of its lipid transfer cavity in proximity to the perpendicular branch of that interface (Figures 7B and 7C). Lipid binding to the perpendicular branch of the protein had been proposed, as has direct lipid transfer from ATG2A to ATG9A; however, a detailed molecular mechanism for the delivery of lipids to the soluble cytoplasmic face of ATG9A was lacking (Guardia et al., 2020; Ghanbarpour et al., 2021; Noda, 2021). Furthermore, mutation of ATG9A R422W, which blocks the perpendicular branch, did not rescue autophagy in ATG9A KO cells (Guardia et al., 2020). Our data and predictive atomic model suggest that lipids are delivered to the perpendicular branch of ATG9A by ATG2A through direct physical interaction and suggest that the failure of the R422W mutant to rescue autophagy is due to the presence of the tryptophan blocking the pathway of lipids between the ATG2A lipid transfer cavity and the cytoplasmic surface of ATG9A (Figure 7B). The reduced solvent accessibility of 9A HDX S2, which is in the perpendicular branch, is also consistent with this hypothesis (Figure 6D).

We speculate that once lipids are bound to the perpendicular branch of ATG9A, they can access the membrane through the central pore or lateral branch in each protomer (Figure 7C). Lipid binding interactions in the solvated environment of these pores is presumably less stable than the lipid-lipid interactions in the lipid bilayer, thermodynamically favoring membrane incorporation of the transferred lipids. The transferred lipids could insert into either the inner or outer leaflet through the lateral opening of the central pore or into the outer leaflet through the lateral branch, initially generating asymmetry which would then be resolved by its scrambling activity. MD simulations of the ATG9A-2A complex in a lipid bilayer would test the plausibility of this hypothesis and facilitate the exploration of this and other potential mechanisms for lipid handover in the ATG9A-2A complex.

In conclusion, using an array of cell biology, biochemical, and biophysical approaches, our study uncovers the molecular details of the interaction between ATG9A and ATG2A and provides mechanistic insight supporting the complex's function in autophagosome biogenesis.

Limitations of the study

Our 3D reconstruction is from NS-EM which can be subject to artifacts due to the dehydration and metal salt staining involved (Thompson et al., 2016). The structure prediction approach using HADDOCK integrated an array of experimental data which was consistent with the low resolution cryo-EM data, but the resulting model only approximates the true atomic arrangement of the complex.

The stoichiometry of the complex we report here may be one of several possibilities, including the possibility that one ATG9A trimer can bind to three ATG2A molecules, and may not reflect the physiological stoichiometry. The validation of our *in vitro* work using cellular models supports the reconstitution and modeling data.

Our use of peptide arrays to look for binding sites has proven successful, but caution is advised. The peptides spotted on the membrane have been taken out of their native protein context

and are assumed to be random coils on the membrane. It may be possible for these peptides to exhibit secondary structure in an aqueous environment, but it is possible we are missing interaction sites that cannot be replicated on a membrane.

The nature of the different ATG9A proteins/mutants of interest used in our stable cell lines led to differing expression levels of each. However, we do not expect this difference to change our interpretation, and this approach supports our conclusion that disruption of the ATG9A-2A interaction leads to impeded autophagic flux. To strengthen these conclusions, when expressed transiently to a similar degree compared with ATG9A WT, ATG9A ΔC22 could not rescue autophagic flux in ATG9A KO cells either.

Our results indicate that ATG9A binding, and membrane binding could be mediated by the same interface in the CLR of ATG2A. This makes it difficult to determine the causative effect of our observed defect in autophagic flux when comparing ATG2A WT with ATG2A ΔS2.

STAR★METHODS

Detailed methods are provided in the online version of this paper and include the following:

- KEY RESOURCES TABLE
- RESOURCE AVAILABILITY
  - ○ Lead contact
  - ○ Materials availability
  - ○ Data and code availability
- EXPERIMENTAL MODEL AND SUBJECT DETAILS
  - ○ Cell lines
- METHOD DETAILS
  - ○ Antibodies
  - ○ Plasmids
  - ○ Immunoprecipitation
  - ○ Western blotting
  - ○ Protein expression and purification
  - ○ Negative stain and cryo-EM grid preparation
  - ○ Negative stain single particle analysis
  - ○ Cryo-EM single particle analysis
  - ○ Peptide array analysis
  - ○ Cross-linking mass spectrometry analysis
  - ○ Immunostaining and confocal microscopy
  - ○ *In vitro* lipid transfer assay
  - ○ *In vitro* lipid scramblase assay
  - ○ Dynamic light scattering assay
  - ○ Hydrogen-deuterium exchange mass spectrometry
  - ○ Modelling of ATG9A-2A complex using HADDOCK
- QUANTIFICATION AND STATISTICAL ANALYSIS

AUTHOR CONTRIBUTIONS

A.R.v.V., G.N.C., and S.A.T. designed the study. A.R.v.V., G.N.C., and C.R. expressed recombinant proteins. A.R.v.V and G.N.C. purified proteins. E.C. provided technical assistance with protein purification. G.N.C. developed protocol for ATG9A purification and 9A-2A complex reconstitution. A.R.v.V. and S.D.T. prepared NS-EM grids. A.R.v.V. and G.N.C. collected NS-EM images. E.P. provided technical assistance with NS-EM imaging. G.N.C. performed image analysis for NS-EM data. V.E.P. prepared cryo-EM grids. P.C. and G.N.C. collected and analyzed cryo-EM data. J.M.S. performed CXL-MS experiments, and J.M.S. and G.N.C. analyzed these data. S.L.M. and J.M.S. performed HDX-MS experiments, and S.L.M. and G.N.C. analyzed these data. A.R.v.V. performed all fluorescence microscopy experiments and in-cell immuno-precipitation, and S.D.T. provided technical assistance with image analysis. J.H.H. produced ATG9A CRIPSR KO cells. H.B.J.J. produced all stable cell lines. G.N.C. performed and interpreted HADDOCK modeling and performed all *in vitro* liposome based activity assays. D.J. and N.O. produced the peptide arrays. A.R.v.V., G.N.C., and S.A.T. wrote the manuscript, and all authors contributed to improving the manuscript.

DECLARATION OF INTERESTS

INCLUSION AND DIVERSITY

REFERENCES

Chowdhury, S., Otomo, C., Leitner, A., Ohashi, K., Aebersold, R., Lander, G.C., and Otomo, T. (2018). Insights into autophagosome biogenesis from structural and biochemical analyses of the ATG2A-WIPI4 complex. Proc. Natl. Acad. Sci. USA *115*, E9792–E9801.

De Vries, S.J., Van Dijk, M., and Bonvin, A.M. (2010). The HADDOCK web server for data-driven biomolecular docking. Nat. Protoc. *5*, 883–897.

Evans, R., O'Neill, M., Pritzel, A., Antropova, N., Senior, A., Green, T., Žídek, A., Bates, R., Blackwell, S., Yim, J., et al. (2022). Protein complex prediction with AlphaFold-Multimer. Preprint at bioRxiv. https://doi.org/10.1101/2021.10.04.463034.

Ghanbarpour, A., Valverde, D.P., Melia, T.J., and Reinisch, K.M. (2021). A model for a partnership of lipid transfer proteins and scramblases in membrane expansion and organelle biogenesis. Proc. Natl. Acad. Sci. USA *118*. 118.10.1073.

Gomez-Sanchez, R., Rose, J., Guimaraes, R., Mari, M., Papinski, D., Rieter, E., Geerts, W.J., Hardenberg, R., Kraft, C., et al. (2018). Atg9 establishes Atg2-dependent contact sites between the endoplasmic reticulum and phagophores. J. Cell Biol. *217*, 2743–2763. https://doi.org/10.1083/jcb.201710116.

Götze, M., Pettelkau, J., Fritzsche, R., Ihling, C.H., Schäfer, M., and Sinz, A. (2015). Automated assignment of MS/MS cleavable cross-links in protein 3D-structure analysis. J. Am. Soc. Mass Spectrom. *26*, 83–97.

Graham, M., Combe, C., Kolbowski, L., and Rappsilber, J. (2019). xiView: A common platform for the downstream analysis of Crosslinking mass spectrometry data. Preprint at bioRxiv. https://doi.org/10.1101/561829.

Grimm, M., Zimniak, T., Kahraman, A., and Herzog, F. (2015). xVis: a web server for the schematic visualization and interpretation of crosslink-derived spatial restraints. Nucleic Acids Res. *43*, W362–W369.

Guardia, C.M., Tan, X.F., Lian, T., Rana, M.S., Zhou, W., Christenson, E.T., Lowry, A.J., Faraldo-Gómez, J.D., Bonifacino, J.S., Jiang, J., et al. (2020). Structure of human ATG9A, the only transmembrane protein of the core autophagy machinery. Cell Rep. *31*, 107837. https://doi.org/10.1016/j.celrep.2020.107837.

Honorato, R.V., Koukos, P.I., Jiménez-García, B., Tsaregorodtsev, A., Verlato, M., Giachetti, A., Rosato, A., and Bonvin, A.M.J.J. (2021). Structural biology in the clouds: the WeNMR-EOSC ecosystem. Front. Mol. Biosci. *8*, 729513.

Judith, D., Jefferies, H.B.J., Boeing, S., Frith, D., Snijders, A.P., and Tooze, S.A. (2019). ATG9A shapes the forming autophagosome through Arfaptin 2 and phosphatidylinositol 4-kinase IIIbeta. J. Cell Biol. *218*, 1634–1652. https://doi.org/10.1083/jcb.201901115.

Karanasios, E., Walker, S.A., Okkenhaug, H., Manifava, M., Hummel, E., Zimmermann, H., Ahmed, Q., Domart, M.C., Collinson, L., and Ktistakis, N.T. (2016). Autophagy initiation by ULK complex assembly on ER tubulovesicular regions marked by ATG9 vesicles. Nat. Commun. *7*, 12420.

Kimanius, D., Forsberg, B.O., Scheres, S.H., and Lindahl, E. (2016). Accelerated cryo-EM structure determination with parallelisation using GPUs in RELION-2. eLife *5*, e18722.

Kopec, J., and Schneider, G. (2011). Comparison of fluorescence and light scattering based methods to assess formation and stability of protein-protein complexes. J. Struct. Biol. *175*, 216–223.

Kosinski, J., Von Appen, A., Ori, A., Karius, K., Müller, C.W., and Beck, M. (2015). Xlink Analyzer: software for analysis and visualization of cross-linking data in the context of three-dimensional structures. J. Struct. Biol. *189*, 177–183. https://doi.org/10.1016/j.jsb.2015.01.014.

Kotani, T., Kirisako, H., Koizumi, M., Ohsumi, Y., and Nakatogawa, H. (2018). The Atg2-Atg18 complex tethers pre-autophagosomal membranes to the endoplasmic reticulum for autophagosome formation. Proc. Natl. Acad. Sci. USA *115*, 10363–10368.

Maeda, S., Otomo, C., and Otomo, T. (2019). The autophagic membrane tether ATG2A transfers lipids between membranes. eLife *8*, e45777.

Maeda, S., Yamamoto, H., Kinch, L.N., Garza, C.M., Takahashi, S., Otomo, C., Grishin, N.V., Forli, S., Mizushima, N., and Otomo, T. (2020). Structure, lipid scrambling activity and role in autophagosome formation of ATG9A. Nat. Struct. Mol. Biol. *27*, 1194–1201.

Matoba, K., Kotani, T., Tsutsumi, A., Tsuji, T., Mori, T., Noshiro, D., Sugita, Y., Nomura, N., Iwata, S., Ohsumi, Y., et al. (2020). Atg9 is a lipid scramblase that mediates autophagosomal membrane expansion. Nat. Struct. Mol. Biol. *27*, 1185–1193.

Melia, T.J., Lystad, A.H., and Simonsen, A. (2020). Autophagosome biogenesis: From membrane growth to closure. J. Cell Biol. *219* 219.10.1083.

Melia, T.J., and Reinisch, K.M. (2022). A possible role for VPS13-family proteins in bulk lipid transfer, membrane expansion and organelle biogenesis. J. Cell Sci. *135* 135.10.1242.

Mercer, T.J., Gubas, A., and Tooze, S.A. (2018). A molecular perspective of mammalian autophagosome biogenesis. J. Biol. Chem. *293*, 5386–5395.

Morishita, H., and Mizushima, N. (2019). Diverse cellular roles of autophagy. Annu. Rev. Cell Dev. Biol. *35*, 453–475.

Neijenhuis, T., Van Keulen, S.C., and Bonvin, A.M.J.J. (2022). Interface refinement of low- to medium-resolution Cryo-EM complexes using HADDOCK2.4. Structure *30*, 476–484.e3. https://doi.org/10.1016/j.str.2022.02.001.

Nishimura, T., and Tooze, S.A. (2020). Emerging roles of ATG proteins and membrane lipids in autophagosome formation. Cell Discov. *6*, 32.

Noda, N.N. (2021). Atg2 and Atg9: intermembrane and interleaflet lipid transporters driving autophagy. Biochim. Biophys. Acta Mol. Cell Biol. Lipids *1866*, 158956.

Orbán-Németh, Z., Beveridge, R., Hollenstein, D.M., Rampler, E., Stranzl, T., Hudecz, O., Doblmann, J., Schlögelhofer, P., and Mechtler, K. (2018). Structural prediction of protein models using distance restraints derived from cross-linking mass spectrometry data. Nat. Protoc. *13*, 478–494.

Orsi, A., Razi, M., Dooley, H.C., Robinson, D., Weston, A.E., Collinson, L.M., and Tooze, S.A. (2012). Dynamic and transient interactions of Atg9 with autophagosomes, but not membrane integration, are required for autophagy. Mol. Biol. Cell *23*, 1860-73. https://doi.org/10.1091/mbc.E11-09-0746.

Osawa, T., Kotani, T., Kawaoka, T., Hirata, E., Suzuki, K., Nakatogawa, H., Ohsumi, Y., and Noda, N.N. (2019). Atg2 mediates direct lipid transfer between membranes for autophagosome formation. Nat. Struct. Mol. Biol. *26*, 281–288.

Pan, D., Brockmeyer, A., Mueller, F., Musacchio, A., and Bange, T. (2018). Simplified protocol for cross-linking mass spectrometry using the MS-cleavable cross-linker DSBU with efficient cross-link identification. Anal. Chem. *90*, 10990–10999.

Pettersen, E.F., Goddard, T.D., Huang, C.C., Couch, G.S., Greenblatt, D.M., Meng, E.C., and Ferrin, T.E. (2004). UCSF Chimera–a visualization system for exploratory research and analysis. J. Comput. Chem. *25*, 1605–1612.

Pettersen, E.F., Goddard, T.D., Huang, C.C., Meng, E.C., Couch, G.S., Croll, T.I., Morris, J.H., and Ferrin, T.E. (2021). UCSF ChimeraX: structure visualization for researchers, educators, and developers. Protein Sci. *30*, 70–82.

Punjani, A., Rubinstein, J.L., Fleet, D.J., and Brubaker, M.A. (2017). cryoSPARC: algorithms for rapid unsupervised cryo-EM structure determination. Nat. Methods *14*, 290–296.

Rodrigues, J.P.G.L.M., Teixeira, J.M.C., Trellet, M., and Bonvin, A.M.J.J. (2018). pdb-tools: a swiss army knife for molecular structures. F1000Res *7*, 1961. https://doi.org/10.12688/f1000research.17456.1.

Rohou, A., and Grigorieff, N. (2015). CTFFIND4: fast and accurate defocus estimation from electron micrographs. J. Struct. Biol. *192*, 216–221.

Sawa-Makarska, J., Baumann, V., Coudevylle, N., von Bülow, S., Nogellova, V., Abert, C., Schuschnig, M., Graef, M., Hummer, G., and Martens, S. (2020). Reconstitution of autophagosome nucleation defines Atg9 vesicles as seeds for membrane formation. Science *369*, eaaz7714.

Scheres, S.H. (2012). RELION: implementation of a Bayesian approach to cryo-EM structure determination. J. Struct. Biol. *180*, 519–530.

Scheres, S.H.W. (2020). Amyloid structure determination in RELION-3.1. Acta Crystallogr. D Struct. Biol. *76*, 94–101.

Schindelin, J., Arganda-Carreras, I., Frise, E., Kaynig, V., Longair, M., Pietzsch, T., Preibisch, S., Rueden, C., Saalfeld, S., Schmid, B., Tinevez, J.Y., White, D.J., Hartenstein, V., Eliceiri, K., Tomancak, P., and Cardona, A. (2012). Fiji: an open-source platform for biological-image analysis. Nat Methods *9*. 676–82. https://doi.org/10.1038/nmeth.2019.

Silva, J.C., Denny, R., Dorschel, C.A., Gorenstein, M., Kass, I.J., Li, G.Z., Mckenna, T., Nold, M.J., Richardson, K., Young, P., and Geromanos, S. (2005). Quantitative proteomic analysis by accurate mass retention time pairs. Anal. Chem. *77*, 2187–2200.

Tamura, N., Nishimura, T., Sakamaki, Y., Koyama-Honda, I., Yamamoto, H., and Mizushima, N. (2017). Differential requirement for ATG2A domains for localization to autophagic membranes and lipid droplets. FEBS Lett. *591*, 3819–3830.

Tang, Z., Takahashi, Y., He, H., Hattori, T., Chen, C., Liang, X., Chen, H., Young, M.M., and Wang, H.G. (2019). TOM40 targets Atg2 to mitochondria-associated ER membranes for phagophore expansion. Cell Rep. *28*, 1744–1757.e5. https://doi.org/10.1016/j.celrep.2019.07.036.

Thompson, R.F., Walker, M., Siebert, C.A., Muench, S.P., and Ranson, N.A. (2016). An introduction to sample preparation and imaging by cryo-electron microscopy for structural biology. Methods *100*, 3–15. https://doi.org/10.1016/j.ymeth.2016.02.017.

Tunyasuvunakool, K., Adler, J., Wu, Z., Green, T., Zielinski, M., Žídek, A., Bridgland, A., Cowie, A., Meyer, C., Laydon, A., et al. (2021). Highly accurate protein structure prediction for the human proteome. Nature *596*, 590–596.

Valverde, D.P., Yu, S., Boggavarapu, V., Kumar, N., Lees, J.A., Walz, T., Reinisch, K.M., and Melia, T.J. (2019). ATG2 transports lipids to promote autophagosome biogenesis. J. Cell Biol. *218*, 1787–1798.

Van Zundert, G.C.P., Rodrigues, J.P.G.L.M., Trellet, M., Schmitz, C., Kastritis, P.L., Karaca, E., Melquiond, A.S.J., Van Dijk, M., De Vries, S.J., and Bonvin, A.M.J.J. (2016). The HADDOCK2.2 web server: user-friendly integrative modeling of biomolecular complexes. J. Mol. Biol. *428*, 720–725. https://doi.org/10.1016/j.jmb.2015.09.014.

Velikkakath, A.K., Nishimura, T., Oita, E., Ishihara, N., and Mizushima, N. (2012). Mammalian Atg2 proteins are essential for autophagosome formation and important for regulation of size and distribution of lipid droplets. Mol. Biol. Cell *23*, 896–909.

Wagner, T., Merino, F., Stabrin, M., Moriya, T., Antoni, C., Apelbaum, A., Hagel, P., Sitsel, O., Raisch, T., Prumbaum, D., et al. (2019). SPHIRE-crYOLO is a fast and accurate fully automated particle picker for cryo-EM. Commun. Biol. *2*, 218.

Wilkins, M.R., Gasteiger, E., Bairoch, A., Sanchez, J.C., Williams, K.L., Appel, R.D., and Hochstrasser, D.F. (1999). Protein identification and analysis tools in the Expasy server. Methods Mol. Biol. *112*, 531–552.

Yamamoto, H., Kakuta, S., Watanabe, T.M., Kitamura, A., Sekito, T., Kondo-Kakuta, C., Ichikawa, R., Kinjo, M., and Ohsumi, Y. (2012). Atg9 vesicles are an important membrane source during early steps of autophagosome formation. J. Cell Biol. *198*, 219–233.

Young, A.R., Chan, E.Y., Hu, X.W., Köchl, R., Crawshaw, S.G., High, S., Hailey, D.W., Lippincott-Schwartz, J., and Tooze, S.A. (2006). Starvation and ULK1-dependent cycling of mammalian Atg9 between the TGN and endosomes. J. Cell Sci. *119*, 3888–3900.

Zhang, K. (2016). Gctf: real-time CTF determination and correction. J. Struct. Biol. *193*, 1–12.

Zhang, Y., Ge, J., Bian, X., and Kumar, A. (2022). Quantitative models of lipid transfer and membrane contact formation. Preprint at bioRxiv. https://doi.org/10.1177/25152564221096024.

Zheng, S.Q., Palovcak, E., Armache, J.P., Verba, K.A., Cheng, Y., and Agard, D.A. (2017). MotionCor2: anisotropic correction of beam-induced motion for improved cryo-electron microscopy. Nat. Methods *14*, 331–332.

Zivanov, J., Nakane, T., Forsberg, B.O., Kimanius, D., Hagen, W.J., Lindahl, E., and Scheres, S.H. (2018). New tools for automated high-resolution cryo-EM structure determination in RELION-3. eLife *7*, e42166.

STAR★METHODS

KEY RESOURCES TABLE

REAGENT or RESOURCE	SOURCE	IDENTIFIER
Antibodies		
Anti-Flag M2	Sigma-Aldrich	Cat. # F3165; RRID:AB_259529
anti-ATG9A (Rabbit)	CRUK (in-house)	N/A
anti-ATG2A	Proteintech	Cat. # 23226; RRID:AB_2879235
anti-GFP (Mouse)	CRUK (in-house)	clone 3E10
anti-Actin (Rabbit)	Abcam	Cat. # ab8227; RRID:AB_2305186
anti-LC3B (Rabbit)	Abcam	Cat. # ab48394; RRID:AB_881433
anti-Myc (Mouse)	CRUK (in-house)	clone 9E10
anti-mouse IgG (HRP conjugated)	GE Healthcare	Cat. # NA931; RRID:AB_772210
anti-rabbit IgG (HRP conjugated)	GE Healthcare	Cat. # NA934; RRID:AB_772206
anti-TGN46 (Sheep)	BioRad	Cat. # AHP500G; RRID:AB_323104
anti-ATG9A (Armenian Hamster)	CRUK (in-house)	Clone 14F28B1
Purified Armenian Hamster IgM Isotype Ctrl Antibody	Biolegend	Cat. #401002
anti-WIPI2 (Mouse)	CRUK (in-house)	Clone 2A2
anti-mouse IgG (Alexa Fluor 555)	Life Technologies	Cat. # A31570; RRID:AB_2536180
anti-rabbit IgG (Alexa Fluor 488)	Life Technologies	Cat. # A11034; RRID:AB_2576217
Chemicals, peptides, and recombinant proteins		
DOPE	Avanti Polar Lipids, Inc	Cat. #850725C
DOPS	Avanti Polar Lipids, Inc	Cat. #840035C
POPC	Avanti Polar Lipids, Inc	Cat. #850457C
POPE	Avanti Polar Lipids, Inc	Cat. #850757C
NBD-PE 18:1	Avanti Polar Lipids, Inc	Cat. #850757C
Rh-PE 18:1	Avanti Polar Lipids, Inc	Cat. #810150C
lauryl maltose neopentyl glycol (LMNG)	Genron	NG310-25GM
cholesteryl hemisuccinate (CHS)	Genron	CH210-5GM
disuccinimidyl dibutyric urea (DSBU)	ThermoFisher Scientific	Cat. # A35459
Polyethyleneimine (PEI, (linear MW 25000))	Polysciences	Cat. #23966-100
3xFlag peptide	Produced in-house	N/A
Luminata Crescendo Western HRP substrate	Merck Millipore	Cat. #WBLUR0500
enhanced chemiluminescence	Merck Millipore	Cat. #RPN2106
anti-DYKDDDDK G1 affinity resin	Genscript	Cat. # L00432
GFP-trap	Chromotech	Cat. #Gta-20
Binding Control Agarose	Chromotech	Cat. #bab-20
cOmplete EDTA free protease inhibitor tablets	Sigma-Aldrich	Cat. #11836170001
Hoechst	Sigma-Aldrich	23491-45-4
Deposited data		
Uncropped Western blot and gel images, raw confocal microscopy images and the integrative model of ATG9A-2A	This paper; Mendeley Data	https://doi.org/10.17632/rrfv4d7jnb.1
ATG9A-2A negative stain 3D reconstruction	This paper; https://www.ebi.ac.uk/emdb/	EMD-15604
ATG2A cryo-EM 3D reconstruction	This paper; https://www.ebi.ac.uk/emdb/	EMD-15605

(Continued on next page)

Continued

REAGENT or RESOURCE	SOURCE	IDENTIFIER
Experimental models: Cell lines		
HEK293A	ThermoFisher Scientific	R70507
HEK293A ATG9A KO	This paper	N/A
HEK293A ATG2AB DKO	Valverde et al., 2019	N/A
Expi293	ThermoFisher Scientific	A14527
Oligonucleotides		
For the entire list of oligonucleotides and synthesized DNA used in this study please see Table S5.	This paper	N/A
Recombinant DNA		
pEGFP-C1	Clontech	N/A
pLVX-Puro	Takara Bio	632164
Myc-ATG2A	David McEwan (Cancer Research UK Beatson Institute)	N/A
Software and algorithms		
Fiji (ImageJ)	Schindelin et al., 2012	https://imagej.net/software/fiji/
RELION v3.1	Scheres, 2012	https://relion.readthedocs.io/en/release-3.1/
CTFFIND4	Rohou and Grigorieff, 2015	https://grigoriefflab.umassmed.edu/ctffind4
crYOLO	Wagner et al., 2019	https://cryolo.readthedocs.io/en/stable
GCTF	Zhang, 2016	https://www2.mrc-lmb.cam.ac.uk/research/locally-developed-software/zhang-software/#gctf
Chimera 1.14	Pettersen et al., 2004	https://www.cgl.ucsf.edu/chimera/
MotionCorr2	Zheng et al., 2017	https://emcore.ucsf.edu/ucsf-software

RESOURCE AVAILABILITY

Lead contact

Further information and requests for resources and reagents should be directed to and will be fulfilled by Sharon Tooze (sharon.tooze@crick.ac.uk).

Materials availability

Plasmids and cell lines generated in this study will be available upon request.

Data and code availability

- Original Western blot data and microscopy images used in this paper have been deposited at Mendeley Data and are publicly available as of the date of publication. The DOI is listed in the key resources table. The negative stain and cryo-EM 3D reconstructions have been deposited in the Electron Microscopy Data Bank (EMDB) with the dataset identifiers EMD-15604 and EMD-15605, respectively. The integrative atomic model of the complex can be downloaded from Mendeley Data.
- This paper does not report original code.
- Any additional information required to reanalyse the data reported in this paper is available from the lead contact upon request.

EXPERIMENTAL MODEL AND SUBJECT DETAILS

Cell lines

HEK293A cells (provided by Cell Services of the Francis Crick Institute) were grown in a humidified incubator at 37 °C in 10% CO_2 in full medium (Dulbecco's modified Eagle's medium supplemented with 10% fetal calf serum and 4 mM L-glutamine). To induce autophagy, cells were washed 3 times with Earle's balanced salt solution (EBSS) and incubated in EBSS for three hours, unless otherwise stated. Where indicated, cells were treated with 100 nM Bafilomycin A1 (Calbiochem) for the specified time. HEK293A stable cells were maintained in full medium + 1 μg/ml puromycin. HEK293A ATG2A/B DKO cells were a kind gift from Prof.

Thomas Melia, (Yale University, USA). Lipofectamine 2000 (Life Technologies) was used for transient transfection of HEK293A cells according to the manufacturer's instructions. DNA plasmid amounts used were in the range of 1-6 μg per 10 cm dish plated to 80% cell confluency.

The ATG9A KO cell line was generated by CRISPR/Cas9-mediated genome engineering using the CRISPR design tool provided by the F. Zhang laboratory (Broad Institute, MIT, Boston, MA). A target sequence in the 2nd exon of human ATG9A was selected (clone 1 sgRNA ATG9A, forward 5′-TTATCAGAACGATTTGGTCG-3′; reverse 5′-CGACCAAATCGTTCTGATAA-3′; and clone 2 sgRNA ATG9A, forward 5′-GGCATCACCCAGTGCATGCT-3′; reverse 5′-AGCATGCACTGGGTGATGCC-3′). The appropriate oligonucleotide was cloned into Bbs1 site of pSpCas9(BB)-2A-GFP plasmid obtained from the laboratory of F. Zhang (Addgene; 48138) according to the cloning protocol provided by the laboratory. Following single-cell sorting on GFP-positive cells, colonies were screened for ATG9A deficiency by immunoblot.

To generate stable cell lines using the ATG2A/B DKO cell line, cell cultures were transduced with Lenti-virus containing empty PLVX-Puro (empty) vector (Takara Bio, Cat. No. 632164), PLVX-Puro-ATG2A WT or PLVX-ATG2A ΔS2. The cell lines were selected with puromycin for 7 days, initially with 3 μg/ml, then 2.5 μg/ml and then maintained in 2.0 μg/ml. ATG2A/B WT cell line was transduced with PLVX-Puro (empty) vector and selected with puromycin as above. The Lenti-viruses were generated by using the Lenti-X 293T cell line (Takara Bio, Cat. No. 632180) transfected with the ATG2A PLVX-Puro constructs or empty vector (as above) using Lenti-X Packaging Single Shots (VSV-G) (Takara Bio., Cat. No. 631275) consisting of Xfect transfection reagent premixed with VSV-G pseudotyped Lenti-X lentiviral packaging plasmids.

To generate stable cell lines using the CRISPR/Cas9 ATG9A KO cell line, cell cultures were transduced with Lenti-virus containing either empty PLVX-Puro vector, PLVX-Puro-ATG9A WT or PLVX-ATG9A ΔC22. The cell lines were selected with puromycin (2.0 μg/ml) for 7 days. The parental ATG9A WT cell line was transduced with empty PLVX-Puro vector and selected with puromycin as above. Lenti-viruses containing the ATG9A PLVX-Puro constructs or empty vector were generated by using the Lenti-X 293T cell line transfected using Lenti-X Packaging Single Shots (VSV-G) as above.

METHOD DETAILS

Antibodies

The following primary antibodies were used for western blot: Anti-Flag M2 (Sigma F3165), rabbit anti-ATG9A (Cancer Research UK (raised in-house)), rabbit anti-ATG2A (Proteintech #23226), mouse anti-GFP (Cancer Research UK (Raised in-house), clone 3E10), rabbit anti-Actin (Abcam, #ab8227), rabbit anti-LC3B (Abcam, #ab48394), mouse anti-Myc (Cancer Research UK (Raised in-house), clone 9E10). HRP-conjugated secondary antibodies used for WB were from GE Healthcare (#NA931 (anti-mouse IgG), #NA934 (anti-rabbit IgG), 1:5000).

The following primary antibodies were used for immunofluorescence (IF): sheep anti-TGN46 (BioRad AHP500G), Armenian hamster anti-ATG9A (Cancer Research UK (Raised in-house)), available from ThermoFischer #MA1-149, rabbit anti-LC3B (Abcam, #ab48394), mouse anti-WIPI2 (Cancer Research UK (Raised in-house)), available from Abcam ab105459.

Secondary antibodies for IF were all from Life Technologies and diluted 1:1000: anti-mouse IgG (IgG) Alexa Fluor 555 (#A31570), anti-rabbit IgG Alexa Fluor 488 (#A11034). Hoechst was from Sigma-Aldrich (23491-45-4).

Plasmids

All plasmids except 3xFlag-His$_6$-ATG9A (Codon optimised, Genscript) subcloned into the pcDNA3.1(+) vector, were generated by PCR and cloned using the In-fusion HD cloning kit (Clontech). GFP-tagged plasmids were generated with the GFP C1 plasmid (Clontech) using the EcoRI and XhoI restriction sites. All deletion mutants were generated using the Q5 Site-Directed Mutagenesis Kit (New England BioLabs). Empty 3xFlag plasmids were generated from GFP C1 plasmids using the AgeI and BamHI restriction sites and inserting 3xFlag with a linker sequence (GSGAGAGAGAILNSRV) and the GFP C1 multiple cloning site. The sequence for full length ATG2A was then cloned using the *EcoR*I and *Xho*I restriction sites. Myc-tagged ATG2A was a kind gift from David McEwan (CRUK Beatson Institute, Glasgow).

The sequences of human ATG9A WT, ΔHelix or ΔC22, and ATG2A WT or ΔS2 were inserted together with a N-terminal 3xFlag-tag in the pLVX-TetOne-Puro vector (Clontech) using EcoRI/XhoI restriction sites.

Immunoprecipitation

Cells were lysed in ice-cold TNTE buffer (20 mM Tris, pH 7.4, 150 mM NaCl, 1% w/v Triton X-100, 5 mM EDTA) modified TNTE buffer (20 mM Tris, pH 7.4, 150 mM NaCl, 1% w/v Triton X-100, 5 mM EDTA, 0.5 mM TCEP, 5% Glycerol) or LMNG buffer (20 mM Tris, pH 7.4, 150 mM NaCl, 1% w/v LMNG, 5 mM EDTA) containing EDTA-free Complete Protease Inhibitor cocktail (Roche). Lysates were cleared by centrifugation at 21000 *g* and precleared with binding control agarose beads (ChromoTek) for 1 h at 4 °C. GFP-tagged proteins were immunoprecipitated using GFP-TRAP beads (ChromoTek) and Flag-tagged proteins with anti-Flag beads (Anti-DYKDDDDK G1 affinity resin from Genscript) ON at 4 °C. Endogenous ATG9A was immunoprecipitated by coupling anti-ATG9A (raised in-house) or control hamster IgM antibodies to protein A Dynabeads® (Sigma). Resin was washed four times with TNTE and bound protein was eluted with 2.5× Laemmli buffer at 100 °C for 5 min before resolving by sodium dodecyl sulfate-polyacrylamide gel electrophoresis (SDS-PAGE) (4–12% Bis-Tris NuPAGE gels, Life Technologies) and western blotting.

Western blotting

Cells were lysed in ice-cold TNTE buffer (20 mM Tris, pH 7.4, 150 mM NaCl, 1% w/v Triton X-100, 5 mM EDTA), modified TNTE buffer (20 mM Tris, pH 7.4, 150 mM NaCl, 1% w/v Triton X-100, 5 mM EDTA, 0.5 mM TCEP, 5% Glycerol) or lauryl maltose neopentyl glycol (LMNG) buffer (20 mM Tris, pH 7.4, 150 mM NaCl, 1% w/v LMNG, 5 mM EDTA) each containing cOmplete EDTA free protease inhibitor tablets (Sigma-Aldrich). Lysates were cleared by centrifugation at 21000g and resolved on NuPAGE®Bis-Tris 4–12% gels (Life Technologies) followed by transfer onto a PVDF membrane (Millipore).

Following incubation with primary and secondary antibodies the blots were developed by enhanced chemiluminescence (GE Healthcare) or with Luminata Crescendo Western HRP substrate (Merck Millipore). Densitometry was performed with ImageQuantTL software (GE Healthcare).

Protein expression and purification

3xFlag-ATG2A and 3xFlag-His$_6$-ATG9A were subcloned into the pcDNA3.1(+) vector for protein expression in Expi293 cells (ThermoFisher). To transfect the cells, polyethyleneimine (linear MW 25000, Polysciences) was mixed and incubated with plasmid DNA for 20 mins in opti-MEM (Thermofisher) at a mass ratio of 3:1 (ATG2A) or 2:1 (ATG9A) and added to the cells in Expi293 expression medium (ThermoFisher) at a cell density of 4×10^6 cells/ml. The transfected cells were harvested after 72 hrs, washed in PBSA buffer, frozen using liquid nitrogen and stored at -80 °C until purification. ATG2A was purified as previously reported (Valverde et al., 2019). Frozen cells expressing ATG2A were thawed in 2A buffer (50 mM HEPES, pH 8, 500 mM NaCl, 10 % w/v glycerol, 1 mM TCEP) supplemented with cOmplete EDTA free protease inhibitor tablets (Sigma-Aldrich). The resuspended cells were lysed by an additional four cycles of freeze-thaw before centrifuging the lysate at 20,000 g for 20 minutes at 4 °C. The supernatant was incubated with anti-DYKDDDDK G1 affinity resin (Genscript) for four hours at 4 °C with mixing before washing the resin with 2A buffer four times. Chaperone removal buffer (50 mM HEPES, pH 8, 500 mM NaCl, 10 % w/v glycerol, 1 mM TCEP, 2.5 mM ATP, 5 mM MgCl$_2$), was added to the washed resin and incubated overnight at 4 °C with mixing. The resin was washed again with 2A buffer and ATG2A eluted by incubating the resin with 240 μg/mL Flag peptide dissolved in 2A buffer.

ATG9A expressing cells were thawed and resuspended in 9A buffer (50 mM Tris, pH 8, 200 mM NaCl) supplemented with 2x cOmplete EDTA free protease inhibitor tablets. A volume equal to this cell suspension of 2.4 % w/v LMNG and cholesteryl hemisuccinate (CHS) mixed at mass ratio of 5:1 in 9A base buffer was added to the suspension to lyse the cells and solubilise ATG9A. Lysis was done for 40 minutes at 4 °C with agitation before removing insoluble material by centrifugation at 4,000 g for 20 minutes. The supernatant was incubated with anti-DYKDDDDK G1 affinity resin for 1 hr at 4 °C with agitation before washing the resin with 9A wash buffer (50 mM Tris, pH 8, 200 mM NaCl, 0.002% w/v LMNG/CHS) supplemented with 2x cOmplete EDTA free protease inhibitor tablets. Elution was done by incubating resin with 240 μg/mL Flag peptide in 9A buffer.

The same protocols were used for purifying the mutants of the two proteins. In the case of ATG9A ΔC22, the buffers were supplemented with 1 mM TCEP and before elution, an overnight chaperone wash in 9A buffer supplemented with 2.5 mM ATP and 5 mM MgCl$_2$, was added. Protein concentrations were calculated by absorbance at 280 nm using molar extinction coefficients of 174495 M^{-1}cm^{-1} and 127200 M^{-1}cm^{-1} for ATG2A and ATG9A respectively, as calculated from the sequences of their constructs (Wilkins et al., 1999). When required, proteins were concentrated using 100 kDa molecular weight cut-off centrifugal concentrators.

To reconstitute the complex, purified ATG2A was supplemented with detergent to a final LMNG/CHS (5:1) concentration of 0.002% and mixed with ATG9A at a molar ratio of 3:1, ATG2A:ATG9A trimer at 4 °C. The sample was passed through a superose 6 size exclusion column equilibrated with 50 mM HEPES, pH 8, 250 mM NaCl, 1 mM TCEP, 0.002% LMNG/CHS (5:1) (9A-2A complex buffer).

Negative stain and cryo-EM grid preparation

ATG2A purified as above was concentrated to 14 mg/mL and run on a superose 6 5 150 column pre-equilibrated with 50 mM HEPES, pH 8, 200mM NaCl, 1mM TCEP. 4 μL of this ATG2A at 0.56 mg/mL, was applied to gold C-flat grids (CF-1.2/1.3-4Au-50 (Electron Microscopy Sciences) under 100% humidity at 22°C, and after a 60 second wait, blotted for 3 seconds and plunge-frozen in liquid ethane using a Vitrobot IV (ThermoScientific Fisher). The ATG9A-2A complex was reconstituted as described above but the LMNG/CHS concentration was reduced to 0.001% w/v during size exclusion. 4 μl of the major peak fraction at 1 mg/ml was applied to gold C-flat grids (CF-1.2/1.3-4Au-50, Electron Microscopy Sciences) under 100% humidity at 22°C, and after a 60 second wait, blotted for 3 seconds and plunge-frozen in liquid ethane using a Vitrobot IV.

For negative stain grid preparation of ATG2A, 9A, and their complex, 3 μl of protein were applied to copper grids with 300 mesh carbon film (Agar scientific) that had been glow discharged for 30 seconds in low air pressure and incubated for 2 minutes. Excess sample was wicked off with filter paper and 2% uranyl acetate applied and left for 5, 10 and a final 15 seconds before finally wicking off the stain and letting grid air-dry.

Negative stain single particle analysis

1847 micrographs were collected with a pixel size of 2.4 Å/pixel, and defocus range of 1 - 1.5 microns on a FEI Tecnai Spirit Twin TEM operated at 120 kV. CTF estimation was done using CTFFind 4.1 (Rohou and Grigorieff, 2015). ~6000 particles were manually picked, extracted, 2D classified and classes chosen as templates for auto picking in RELION 3.1 (Scheres, 2012; Zivanov et al., 2018). After removing micrographs with bad CTF estimates, 1506 micrographs were auto picked using templates yielding 88107 particles. These

were extracted, 2.5 times binned, and 2D classified, during which CTFs were ignored until first peak. 12361 particles were selected after 2D classification, re-extracted at full resolution, and used to generate an initial 3D model by stochastic gradient descent in RELION 3.1. After two rounds of 3D classification, 2058 particles were selected for 3D refinement. A mask was generated from the resulting map and used for post processing in RELION 3.1. EM map docking, visualization and figures were prepared using UCSF Chimera and Chimera X (Pettersen et al., 2004, 2021).

Cryo-EM single particle analysis

Particles of ATG9A-2A complex were imaged on a Krios microscope (FEI) operating at 300 keV and equipped with a K2 Summit direct electron detector (Gatan) and a BioQuantum energy filter (Gatan). In total, 17,816 micrograph movies were collected at a calibrated magnification of 46,296, resulting in a pixel size of 1.08 Å at the specimen level, 20 eV energy filter slit, a nominal defocus range -1 to -3 μm, and a total dose of 48.3 electrons per $Å^2$ spread over 32 frames. The micrograph stacks were aligned and summed applying dose weighting as implemented in MotionCor2 (Zheng et al., 2017), and contrast transfer function (CTF) parameters were estimated using Gctf (Zhang, 2016). The particles, initially picked with crYOLO (Wagner et al., 2019), were subjected to reference-free 2D classification in cryoSPARC (Punjani et al., 2017). The best defined 2D class averages, low pass filtered to 20 Å were used as templates to pick the dataset with Gautomatch (http://www.mrc-lmb.cam.ac.uk/kzhang/). The resulting set of 994,751 particles binned to a pixel size of 4.32 $Å^2$ were subjected to several rounds of reference-free 2D classification in cryoSPARC. Examples of the resulting 2D class averages are shown in Figure 1E. Due to extensive conformational variability, further image processing and classification did not result in a reliable 3D reconstruction.

Particles of free ATG2A were imaged using a Talos Arctica microscope (FEI) operating at 200 keV, using a Falcon III direct electron detector (Gatan). In total, 2,287 micrograph stacks were acquired at a calibrated magnification of 111,111 and a pixel size of 1.26 Å. Data collection was conducted in using the linear integration mode of the Falcon III detector, with a defocus range of -1.0 to -3.5 μm, and a total dose of 80 electron per $Å^2$ spread over 10 frames. The micrograph stacks were aligned and summed with dose weighting using MotionCor2; and CTF parameters were estimated with Gctf. Particles, initially picked with crYOLO, were subjected to reference-free 2D classification in RELION 3.1 (Scheres, 2020; Kimanius et al., 2016). Three best-defined 2D class averages, low pass filtered to 20 Å, were then used as templates to pick the entire dataset with Gautomatch (http://www.mrc-lmb.cam.ac.uk/kzhang/). The resulting 1,101,546 particles, extracted binned to a pixel size 5.04 Å, were subjected to four rounds of reference-free 2D classification cryoSPARC. Each round, particles were classified into 200 classes over 50 iterations, and well-defined classes were selected for the next round of classification. The final subset of 42,235 particles contributing the best-defined averages (Figure 2B) was re-extracted with a pixel size 2.52 Å and used for 3D auto-refinement in RELION 3.1 (Figure 2B). The starting model was generated using Ab-initio reconstruction in cryoSPARC. Due to low resolution, the hand of the reconstruction remained ambiguous.

Peptide array analysis

Peptide arrays were synthesised on an Intavis ResPepSL Automated Peptide Synthesiser (Intavis Bioanalytical Instruments, Germany, now owned by CEM) on a cellulose membrane by cycles of N(a)-Fmoc amino acids coupling via activation of carboxylic acid groups with diisopropylcarbodiimide (DIC) in the presence of Ethyl cyano(hydroxyimino)acetate (Oxyma pure) or HOBT followed by removal of the temporary α-amino protecting group by piperidine treatment. After chain assembly, side chain protection groups are removed by treatment of membranes with a deprotection cocktail (20 mls 95% trifluoroacetic acid, 3% triisopropylsilane 2% water 4h at RT) then washing (4 x DCM, 4 X EtOH 2x H20, 1 x EtOH) prior to being air dried. 3xFlag-ATG9A or 3xFlag only proteins were incubated ON with anti-Flag M2 antibody at a 1:1 weight ratio. After blocking membranes in TBS-Tween with 5% non-fat dry milk, peptide interactions with 3xFlag-ATG9A or 3xFlag protein-antibody complex were tested by overlaying the membranes with 1 μg/ml protein-antibody complex for 2 h at room temperature in TBS-Tween. Membranes were washed in TBS-Tween and incubated ON with HRP-conjugated anti-mouse antibody (1:5000, GE Healthcare, RPN1236) in TBS-Tween with 5% non-fat dry milk. Membranes were washed 4 times with TBS-Tween and developed by enhanced chemiluminescence (GE Healthcare) or with Luminata Crescendo Western HRP substrate (Merck Millipore).

Cross-linking mass spectrometry analysis

The ATG9A-2A complex was reconstituted as described above and exchanged into 9A-2A complex buffer supplemented with glycerol to a final concentration of 10 % w/v by size exclusion chromatography on a superose 6 5 150 column. The complex peak fraction was cross-linked with a 100-fold excess of the N-hydroxysuccinimide (NHS) ester disuccinimidyl dibutyric urea (DSBU, ThermoScientific, USA), with respect to the protein concentration. The cross-linking reactions were incubated for 60 minutes at room temperature and then quenched by the addition of NH_4HCO_3 to a final concentration of 20 mM and incubated for further 15 min.

The cross-linked proteins were reduced with 10 mM DTT and alkylated with 50 mM iodoacetamide. Following alkylation, the proteins were digested with trypsin (Promega, UK) at an enzyme-to-substrate ratio of 1:100, for 1 hour at room temperature and then further digested overnight at 37 °C following a subsequent addition of trypsin at a ratio of 1:20.

The peptide digests were then fractionated batch wise by high pH reverse phase chromatography on micro spin C18 columns (Harvard Apparatus, USA), into four fractions (10 mM NH_4HCO_3 /10 % (v/v) acetonitrile pH 8, 10 mM NH_4HCO_3 /20 % (v/v) acetonitrile

pH 8, 10 mM NH_4HCO_3 /40 % (v/v) acetonitrile pH 8 and 10 mM NH_4HCO_3/80 % (v/v) acetonitrile pH 8. The 150 µl fractions were evaporated to dryness in a CentriVap concentrator (Labconco, USA) prior to analysis by LC-MS/MS.

Lyophilized peptides for LC-MS/MS were resuspended in 0.1 % (v/v) formic acid and 2 % (v/v) acetonitrile and analysed by nano-scale capillary LC-MS/MS using an Ultimate U3000 HPLC (ThermoScientific Dionex, USA) to deliver a flow of approximately 275 nl/min. A C18 Acclaim PepMap100 5 µm, 100 µm × 20 mm nanoViper (ThermoScientific Dionex, USA), trapped the peptides before separation on a 50 cm EASY-Spray column (50 cm × 75 µm ID, PepMap C18, 2 µm particles, 100 Å pore size (ThermoScientific, USA). Peptides were eluted with a gradient of acetonitrile. The analytical column outlet was directly interfaced via a nano-flow electrospray ionisation source, with a quadrupole Orbitrap mass spectrometer (Orbitrap Eclipse Tribrid, ThermoScientific, USA). MS data were acquired in data-dependent mode using a top 10 method, where ions with a precursor charge state of 1+ and 2+ were excluded. High-resolution full scans (R=60 000, m/z 300-1800) were recorded in the Orbitrap followed by higher energy collision dissociation (HCD) (stepped collision energy 26 and 28 % Normalized Collision Energy) of the 10 most intense MS peaks. The fragment ion spectra were acquired at a resolution of 30 000 and dynamic exclusion window of 20s was applied.

For data analysis, Xcalibur raw files were converted into the MGF format using Proteome Discoverer version 2.3 (ThermoScientific, USA) and used directly as input files for MeroX (Götze et al., 2015). Searches were performed against an ad hoc protein database containing the sequences of the proteins in the complex and a set of randomized decoy sequences generated by the software. The following parameters were set for the searches: maximum number of missed cleavages 3; targeted residues K, S, Y and T; minimum peptide length 5 amino acids; variable modifications: carbamidomethylation of cysteine (mass shift 57.02146 Da), Methionine oxidation (mass shift 15.99491 Da); DSBU modified fragments: 85.05276 Da and 111.03203 Da (precision: 5 ppm MS and 10 ppm MS/MS); False Discovery Rate cut-off: 5 %. Finally, each fragmentation spectrum was manually inspected and validated.

Crosslinks were analysed using xiView and visualisation done using xVis and the Xlink Analyzer (Graham et al., 2019; Grimm et al., 2015; Kosinski et al., 2015). Crosslinks were filtered by match score (>273) and interprotein crosslinks by their distance in the AF model docked 3D reconstruction of the map (<100 Å).

Immunostaining and confocal microscopy

Cells were grown and treated on coverslips, and then fixed with 3% paraformaldehyde in phosphate-buffered saline (PBS) for 10 min before permeabilization with methanol or 50 µg/ml digitonin in PBS at room temperature for 5 min. Coverslips were then washed with PBS and blocked in 5% BSA (Roche) in PBS for 20 min. Coverslips were incubated with primary antibody in 5% BSA in PBS 1 h at room temperature. Coverslips were washed and incubated with secondary antibody in 5% BSA for 1 h. After final washing with PBS and demineralized water, coverslips were mounted in mowiol. Images were acquired using a Zeiss LSM 880 Airyscan Confocal microscope (×40 oil-immersion lens) and Zeiss ZEN imaging software. LC3 and WIPI2 puncta Image analysis was performed using the analyse particle function of ImageJ after thresholding the images.

In vitro lipid transfer assay

1,2-dioleoyl-sn-glycero-3-phosphocholine (DOPC), 1,2-dioleoyl-sn-glycero-3-phosphoethanolamine (DOPE), 1,2-dioleoyl-sn-glycero-3-phosphoethanolamine-N-(7-nitro-2-1,3-benzoxadiazol-4-yl) (ammonium salt) (NBD-PE), 1,2-dioleoyl-sn-glycero-3-phosphoethanolamine-N-(lissamine rhodamine b sulfonyl) (ammonium salt) (Rh-PE) were mixed at a molar ratio of 71:25:2:2 respectively for the donor liposomes, the chloroform they were dissolved in was evaporated using a N_2 gas stream then the lipids dried further under vacuum for an hour (Avanti Polar Lipids). The acceptor liposomes mix was prepared similarly but using 75:25 DOPC: DOPS instead. The dried lipid mixtures were resuspended in 80 mM HEPES, 150 mM NaCl, pH 7.5 (liposome buffer) at a final total lipid concentration of 3 mM and agitated for 30 minutes before subjecting to 3 cycles of flash freeze-thaw. This was followed by extrusion 21 times through a 100 nm pore filter (Whatman). Liposome size was checked by dynamic light scattering (DLS) before use in the assay.

For the assay, final lipid concentration of each lipid mix was 25 µM for both donor and acceptor liposomes. The samples were excited at 452 nm and NBD fluorescence measured at 538 nm. NBD fluorescence was measured for 120 seconds before adding purified ATG2A WT or mutant to final concentration of 100 nM or 250 nM before resuming measurement for another 3600 seconds followed by adding 1 mM dithionate to a final concentration of 48 µM, to control for liposome fusion. The rate of NDB-PE transfer was calculated by determining the slope of the linear regression of the fluorescence plotted against time.

In vitro lipid scramblase assay

1-palmitoyl-2-oleoyl-sn-glycero-3-phosphocholine (POPC), DOPS and 1-palmitoyl-2-oleoyl-sn-glycero-3-phosphoethanolamine (POPE) (Avanti Polar Lipids) at a molar ratio of 95.5:5:0.5 in chloroform then dried under N_2 and for an hour under vacuum. The lipid mix was resuspended in liposome buffer and mixed for 30 minutes before three cycles of flash freeze-thaw. 200 liposomes were generated by extrusion of the lipid mix 21 times through a 400 nm filter. The diameter of the liposomes was checked by DLS before setting up the proteoliposome reconstitution. For proteoliposome reconstitution, purified ATG9A WT or mutant was incubated at 55 nM, with 654 µM lipid mix and 0.44 % w/v Triton-X100 in proteoliposome reconstitution buffer (liposome buffer supplemented with TCEP to a final concentration 0.3 mM. The reconstitution reaction was incubated for one hour at 4 °C with agitation. Bio-beads

SM2 (Bio-Rad) washed with methanol, water and finally proteoliposome reconstitution buffer were added to the reconstitution mix and incubated over night with agitation.

For the assay the proteoliposomes were diluted 1:10.4 with proteoliposome buffer, before measuring NBD-PE fluorescence; excitation 452 nm, emission 538 nm. After 100 seconds of measurement, dithionate was added to a final concentration of 20 μM and fluorescence measured for another 400 seconds. Δ Normalized fluorescence was calculated by subtracting the fluorescence of the proteoliposome conditions from that of the no protein control at 200 seconds, this value (Δ fluorescence) was then divided by that of the Δ fluorescence of the ATG9A WT value.

Dynamic light scattering assay

DOPC and DOPS dissolved in chloroform were mixed at a molar ratio of 75:25 respectively and dried by N_2 stream followed by an hour under vacuum. The dried lipids were resuspended in liposome buffer by mixing for 30 minutes before 3 cycles of freeze-thaw to make unilamellar liposomes. Small unilamellar vesicles (∼60 – 80 nm) were generated by sonicating the liposomes and size was determined by DLS. 60 μM SUV was incubated with 200 nM purified wild type 3xFlag-ATG2A or mutant proteins for 20 minutes before measuring size again by DLS.

Hydrogen-deuterium exchange mass spectrometry

Individual proteins or complex (5μM) were incubated with 40 μL of D2O buffer at room temperature for 30, 300 and 3000 seconds in triplicate. The labelling reaction was quenched by adding chilled 2.4% v/v formic acid in 2M guanidinium hydrochloride and immediately frozen in liquid nitrogen. Samples were stored at -80°C prior to analysis.

The quenched protein samples were rapidly thawed and subjected to proteolytic cleavage by pepsin followed by reversed phase HPLC separation. Briefly, the protein was passed through an Enzymate BEH immobilized pepsin column, 2.1 x 30 mm, 5 μm (Waters, UK) at 200 μL/min for 2 min and the peptic peptides trapped and desalted on a 2.1 x 5 mm C18 trap column (Acquity BEH C18 Vanguard pre-column, 1.7 μm, Waters, UK). Trapped peptides were subsequently eluted over 12 min using a 5-36% gradient of acetonitrile in 0.1% v/v formic acid at 40 μL/min. Peptides were separated on a reverse phase column (Acquity UPLC BEH C18 column 1.7 μm, 100 mm x 1 mm (Waters, UK). Peptides were detected on a SYNAPT G2-Si HDMS mass spectrometer (Waters, UK) acquiring over a m/z of 300 to 2000, with the standard electrospray ionization (ESI) source and lock mass calibration using [Glu1]-fibrino peptide B (50 fmol/μL). The mass spectrometer was operated at a source temperature of 80°C and a spray voltage of 3.0 kV. Spectra were collected in positive ion mode.

Peptide identification was performed by MSe (Silva et al., 2005) using an identical gradient of increasing acetonitrile in 0.1% v/v formic acid over 12 min. The resulting MSe data were analysed using Protein Lynx Global Server software (Waters, UK) with an MS tolerance of 5 ppm.

Mass analysis of the peptide centroids was performed using DynamX sotware (Waters, UK). Only peptides with a score >6.4 were considered. The first round of analysis and identification was performed automatically by the DynamX software, however, all peptides (deuterated and non-deuterated) were manually verified at every time point for the correct charge state, presence of overlapping peptides, and correct retention time. Deuterium incorporation was not corrected for back-exchange and represents relative, rather than absolute changes in deuterium levels. Changes in H/D amide exchange in any peptide may be due to a single amide or several amides within that peptide. All time points in this study were prepared at the same time and individual time points were acquired on the mass spectrometer on the same day.

Modelling of ATG9A-2A complex using HADDOCK

AlphaFold multimer prediction of the complex was attempted using a local version of the program however this did not yield meaningful results, so we leveraged our experimental data in HADDOCK (Evans et al., 2022; Honorato et al., 2021; van Zundert et al., 2016). Regions of the AlphaFold (AF) models of ATG9A (AF-Q7Z3C6-F1-model_v1) and ATG2A (AF-Q2TAZ0-F1-model_v1) that have per residue confidence scores less than 50 were removed. The ATG9A trimer was generated through duplication and alignment with PDB 6WQZ. The models were docked into the complex NS-EM 3D reconstruction and the atomic models saved oriented relative to the map. ATG2A was truncated to residues 770–1934 and the ATG9A AF trimer concatenated into a single chain with residues renumbered sequential so that there was no overlap. Docking was done through the HADDOCK 2.4 web interface where the structures were uploaded, their orientation not fixed during it0 and coarse grained during the docking. Active residues in ATG9A were defined in what would be the second protomer before concatenation, as 801-821, 942-952, 1156-1172, corresponding to 9A HDX sites 1,3 and 4 and passive residues were defined as 781,773,1189. In ATG2A active residues were defined as 1736-1757 and 1805-1810, passive residues as 1539,1546,1880,1930 (Figures S8A and S8B). Random exclusion of AIRS was turned on and default value 2 used, and where not stated the default settings were used. HADDOCK clustered 151 structures in 9 clusters, the best scoring was cluster 1 which had 52 structures with a HADDOCK score -92.5 +/- 3.9 and iRMSD = 1.3 Å. The best scoring model was used to generate the full complex by aligning it with the ATG9A trimer and ATG2A AF models prepared as described above and then these were saved as a single model. Another full-length model was generated similarly using the experimental structure of ATG9A (PDB ID 6WQZ) instead of the AF model. The interfaces were refined using HADDOCK 2.4's coarse grain refinement procedure via the web server (Neijenhuis et al., 2022). Model quality was assessed at various steps during the modelling and in the final models by determining how well the models satisfied the CXL-MS derived distance constraints and binding site data from

HDX-MS and mutagenesis (Figures S8A and S8B; Table S2; Video S1). Consistency with PDB file format for files used for and docking and refinement was ensured using PDB-tools (Rodrigues et al., 2018). EM map docking, visualization and figures were prepared using UCSF Chimera and Chimera X (Pettersen et al., 2004, 2021).

QUANTIFICATION AND STATISTICAL ANALYSIS

The statistical details of all experiments are reported in the figure legends and figures, including statistical analysis performed, error bars, statistical significance, and exact n numbers. Statistics were performed using GraphPad Prism 7 software, as detailed in figure legends.